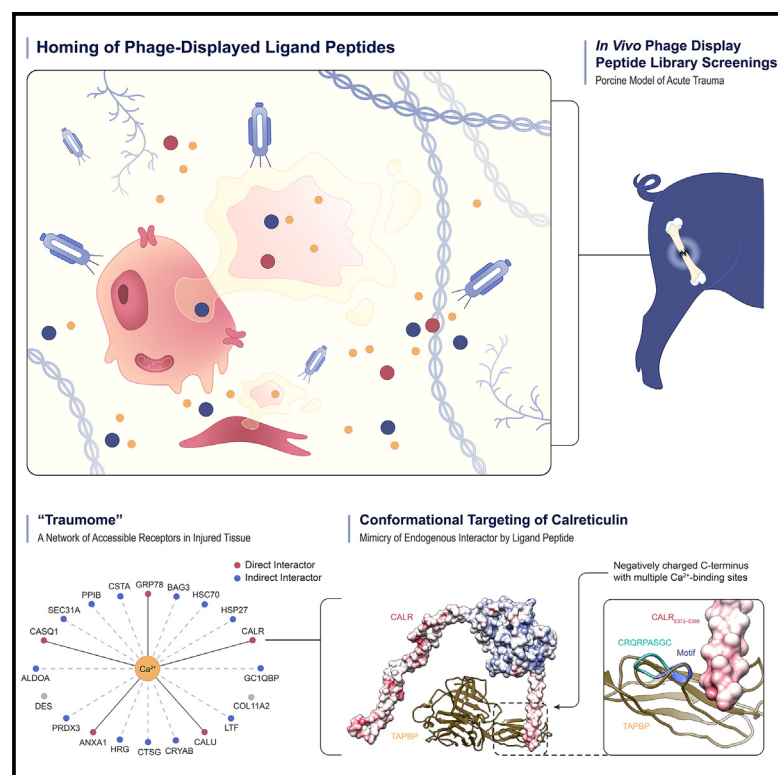# Conformational ligand-directed targeting of calcium-dependent receptors in acute trauma

Graphical abstract

Authors

Renata Pasqualini,
Christopher Markosian,
Daniela I. Staquicini, ...,
Stephen K. Burley, José N. Onuchic,
Wadih Arap

Correspondence

renata.pasqualini@rutgers.edu (R.P.),
wadih.arap@rutgers.edu (W.A.)

In brief

Major trauma is a leading cause of death worldwide; however, translational targets have not been systematically identified. Pasqualini et al. identify a repertoire of trauma-homing ligand peptides targeting unique conformations of calcium-dependent receptors (as part of the trauma-related proteome, henceforth "traumome"), and advance one such ligand-receptor system toward translational applications.

Highlights

- Pool of ligand peptides (n = 23) specifically homing to compound femur fracture

- Trauma targets (trauma-related proteome or "traumome") largely calcium dependent

- CRQRPASGC:calreticulin (CALR) translated toward molecular imaging applications

- CRQRPASGC targets a calcium-facilitated spatial and temporal conformation of CALR

Pre-clinical Research

CellPress

Med

Article

Conformational ligand-directed targeting of calcium-dependent receptors in acute trauma

Renata Pasqualini,[1,2,47,48,*] Christopher Markosian,[1,2,46] Daniela I. Staquicini,[1,2,46] Andrey S. Dobroff,[3,4,39,46]
Esteban Dodero-Rojas,[5,46] Paul C. Whitford,[6,7,46] E. Magda Barbu,[3,4,40] Julianna K. Bronk,[8] Marina Cardó-Vila,[9,10]
Dawn R. Christianson,[3,4,41] Emmanuel Dias-Neto,[1,2,11] Wouter H.P. Driessen,[3,4,42] Liliana Guzman-Rojas,[12]
Serena Marchiò,[13] Diana N. Nunes,[1,2,11] Francislon S. de Oliveira,[14] Michael G. Ozawa,[15] Bettina Proneth,[16]
Roberto Rangel,[17] Tracey L. Smith,[1,2] Glauco R. Souza,[3,4,43] Fernanda I. Staquicini,[1,2,44] Fenny H.F. Tang,[1,2]

(Author list continued on next page)

[1]Rutgers Cancer Institute, Newark, NJ, USA
[2]Division of Cancer Biology, Department of Radiation Oncology, Rutgers New Jersey Medical School, Newark, NJ, USA
[3]David H. Koch Center, Houston, TX, USA
[4]Department of Genitourinary Medical Oncology, University of Texas MD Anderson Cancer Center, Houston, TX, USA
[5]Center for Theoretical Biological Physics, Rice University, Houston, TX, USA
[6]Center for Theoretical Biological Physics, Northeastern University, Boston, MA, USA
[7]Department of Physics, Northeastern University, Boston, MA, USA
[8]Department of Radiation Oncology, University of Texas MD Anderson Cancer Center, Houston, TX, USA
[9]Department of Cellular & Molecular Medicine, University of Arizona Cancer Center, University of Arizona, Tucson, AZ, USA
[10]Department of Otolaryngology and Head & Neck Surgery, University of Arizona Cancer Center, University of Arizona, Tucson, AZ, USA
[11]Laboratory of Medical Genomics, A.C. Camargo Cancer Center, São Paulo, SP, Brazil
[12]Cancer Research Program, Houston Methodist Research Institute, Houston, TX, USA
[13]Department of Oncology, University of Turin, Candiolo, TO, Italy
[14]Department of Biochemistry, Institute of Chemistry, University of São Paulo, São Paulo, SP, Brazil
[15]Department of Pathology, Stanford University School of Medicine, Stanford, CA, USA
[16]Institute of Metabolism and Cell Death, Helmholtz Center Munich, Neuherberg, BY, Germany
[17]Department of Head & Neck Surgery, University of Texas MD Anderson Cancer Center, Houston, TX, USA

(Affiliations continued on next page)

CONTEXT AND SIGNIFICANCE Major trauma is a leading cause of severe disability and death, yet molecular targets unique to such settings have not been systematically identified. By screening a porcine model of acute trauma with phage display libraries, the authors identified a collection of trauma-specific ligand peptides. They discovered that their corresponding receptors (as part of the trauma-related proteome, henceforth, "traumome") are largely calcium dependent and become readily accessible after trauma. The authors demonstrated that ligand peptide CRQRPASGC, which homes *in vivo* and binds to a trauma-specific calcium-enabled protein conformation of calreticulin, can serve as a targeted molecular imaging agent for tissue injury in live animals. These discoveries conceptually advance the understanding of trauma biology and pave the way for targeted theragnostic interventions.

SUMMARY

Background: Trauma is a leading cause of mortality, but injury-specific molecular targets remain largely unknown. We hypothesized that distinctive yet unrecognized tissue targets accessible to circulating ligands might emerge during trauma, thereby underscoring a trauma-related proteome.
Methods: We screened a peptide library to discover targets in a porcine model of major trauma: compound femur fracture with hemorrhagic shock. Bioinformatics yielded conserved motifs, and candidate receptors were affinity purified. *In silico* and *in vitro* approaches served to investigate possible associations between candidate receptors and calcium, a major component of skeletal muscle and bone. *In vivo* homing and molecular imaging (PET/MRI and SPECT/CT) studies of the most promising ligand peptide candidate were

Wallace B. Baze,[18] João C. Setubal,[14] John W. Burns,[19,45] Michael A. Dubick,[19,45] Juri G. Gelovani,[20,21,22,23] Andriy I. Batchinsky,[24] Jon E. Mogford,[25] Charles E. Wade,[26,27,28] John B. Holcomb,[29,30] Stephen K. Burley,[31,32,33,34] José N. Onuchic,[5,35,36,37] and Wadih Arap[1,38,47,*]

[18]Keeling Center for Comparative Medicine & Research, Department of Comparative Medicine, University of Texas MD Anderson Cancer Center, Bastrop, TX, USA
[19]US Army Institute of Surgical Research, Fort Sam Houston, TX, USA
[20]Office of the Provost, United Arab Emirates University, Al Ain, Abu Dhabi, UAE
[21]Department of Radiology, College of Medicine & Health Sciences, United Arab Emirates University, Al Ain, Abu Dhabi, UAE
[22]Department of Radiology, Siriraj Hospital, Mahidol University, Bangkok, Thailand
[23]Department of Biomedical Engineering, College of Engineering and School of Medicine, Wayne State University, Detroit, MI, USA
[24]Autonomous Reanimation & Evacuation (AREVA) Research Institute and Innovation Center, The Geneva Foundation, San Antonio, TX, USA
[25]Defense Sciences Office, Defense Advanced Research Projects Agency, Arlington, VA, USA
[26]Center for Translational Injury Research, Department of Surgery, McGovern Medical School at the University of Texas Health Science Center, Houston, TX, USA
[27]CAG Center for Endotheliomics, Copenhagen University Hospital – Rigshospitalet, Copenhagen, Denmark
[28]Department of Clinical Medicine, University of Copenhagen, Copenhagen, Denmark
[29]Center for Injury Science, University of Alabama at Birmingham, Birmingham, AL, USA
[30]Division of Acute Care Surgery, Department of Surgery, University of Alabama at Birmingham, Birmingham, AL, USA
[31]RCSB Protein Data Bank, Rutgers, The State University of New Jersey, Piscataway, NJ, USA
[32]RCSB Protein Data Bank, San Diego Supercomputer Center, University of California, San Diego, La Jolla, CA, USA
[33]Institute for Quantitative Biomedicine, Rutgers, The State University of New Jersey, Piscataway, NJ, USA
[34]Rutgers Cancer Institute, New Brunswick, NJ, USA
[35]Department of Biosciences, Rice University, Houston, TX, USA
[36]Department of Chemistry, Rice University, Houston, TX, USA
[37]Department of Physics & Astronomy, Rice University, Houston, TX, USA
[38]Division of Hematology/Oncology, Department of Medicine, Rutgers New Jersey Medical School, Newark, NJ, USA
[39]Present address: NextRNA Therapeutics, Boston, MA, USA
[40]Present address: Amazon.com, Seattle, WA, USA
[41]Present address: Vividion Therapeutics, San Diego, CA, USA
[42]Present address: Anjarium Biosciences, Schlieren, ZH, Switzerland
[43]Present address: Greiner Bio-One North America, Monroe, NC, USA
[44]Present address: MBrace Therapeutics, North Brunswick Township, NJ, USA
[45]Deceased
[46]These authors contributed equally
[47]Senior author
[48]Lead contact
*Correspondence: renata.pasqualini@rutgers.edu (R.P.), wadih.arap@rutgers.edu (W.A.)
https://doi.org/10.1016/j.medj.2025.100638

performed in the porcine model and were also confirmed in a corresponding rat model of major trauma. Optical methodologies and molecular dynamics simulations served to explore the molecular attributes of the ligand-receptor binding.

Findings: Nearly all molecular targets of the selected ligand peptides were calcium-dependent proteins, which become accessible upon trauma. We validated specific binding of homing peptides to these receptors in injured tissues, including CLRGFPALVC:CASQ1, CSEIGVRAC:HSP27, and CRQRPASGC:CALR. Notably, we determined that ligand peptide CRQRPASGC targets an injury-specific calcium-facilitated conformation of calreticulin, enabling specific molecular imaging of trauma.

Conclusions: We conceptually propose the term "traumome" for the functional receptor repertoire that becomes readily amenable for ligand-directed targeting upon major trauma. These preclinical findings pave the way toward clinic-ready targeted theragnostic approaches in the setting of trauma.

Funding: Major funding was provided by the Defense Advanced Research Projects Agency (DARPA).

INTRODUCTION

Major trauma is a leading cause of severe disability and death worldwide, either in civilian life or on the battlefield.[1] Despite the high frequency of trauma-related injuries globally, molecular targets unique to such settings have not yet been systematically identified. This is a critical and contemporary unmet need since blunt and penetrating trauma are often challenging to manage.

The mammalian vascular system responds to physiologic and pathologic stimuli by differential regulation and expression of unique, circulation-accessible, organ-specific, and angiogenesis-related endothelial receptors.[2] Efforts to map ligand-receptors in blood vessels have led to the discovery of an

unanticipated, vast vascular endothelial cell-surface diversity with functional attributes that serve as the basis for the understanding of biological function and development of targeted therapy.[3–7] *In vivo* phage display technology holds promise for discovering molecular targets within the complex biological microenvironment of major trauma. Our group has long investigated the organ-specific molecular diversity of the vascular endothelium and lymphatic channels under physiologic and pathologic conditions—such as cancer and obesity—to identify and exploit such cell surface-accessible ligand-receptor systems.[3,4,7–13] While this approach has not previously been applied to severe musculoskeletal trauma, we reasoned that its acute disruption of tissue architecture and release of intracellular content would provide an opportunity to uncover protein interactions specific to tissue injury. If so, one could adapt ligand-directed targeting of functional protein-protein interactions at injury sites for translational applications, such as reducing trauma-induced damage, controlling bleeding, and promoting tissue repair.

Herein, we identified a panel of ligand peptides that selectively accumulated in injured tissue of a porcine model, specifically compound femur fracture with hemorrhagic shock.[14] Surprisingly, we found that nearly all biochemically isolated receptors were calcium (Ca^{2+})-dependent proteins, which may facilitate immediate ligand-directed targeting. The molar concentration of extracellular Ca^{2+} can be >10,000-fold higher than intracellular Ca^{2+} under physiological conditions.[15] Therefore, we have hypothesized that the pool of intracellular Ca^{2+}-dependent proteins released upon major trauma would promptly change their conformations upon Ca^{2+} binding when encountering this marked differential cation gradient. These results provide evidence for a hitherto unrecognized, rapidly inducible network of Ca^{2+}-dependent proteins that allow conformational targeting as part of an overarching trauma-related proteome. Conceptually, we propose the term "traumome" to designate these empiric findings and biological phenomenon at large.

RESULTS

Phage display peptide library selection in a porcine model of acute trauma

To identify trauma-associated molecular targets, *in vivo* screenings of ligand peptides were performed in a porcine model of acute trauma (*n* = 4)[14] comprising compound femur fracture with bone and soft tissue injury plus hemorrhagic shock (Figure 1A). A phage display cyclic peptide library was infused intravenously (IV) with a serial collection of blood and tissue biopsies at fixed time points (up to 4 h post-infusion), followed by euthanasia and necropsy (Figure 1B); non-injured pigs (*n* = 4) under the same experimental conditions served as negative controls (Figures S1A–S1C).

To analyze differential tissue homing of peptide-targeted phage particles, collected samples were processed for quantitative PCR (qPCR) and next-generation sequencing (NGS). Phage particle kinetics in the circulation (Figure 1C) and tissue biopsy (Figure 1D) plus necropsy samples (Figure 1E) from the injured animals (i.e., experimental fractured hindleg versus contralateral intact hindleg) demonstrates their clearance from the blood and

retention of a subset within the collected tissues. This large-animal protocol provides an experimental framework for *in vivo* recovery of ligand peptides from injury sites, peripheral blood, and control tissues, including mononuclear phagocytic system-rich organs such as liver and spleen.

High-throughput analysis of ligand peptide-encoding DNA sequences

DNA-encoded ligand peptides from the samples of experimental (injured) or contralateral (intact) control hindlegs of the injured pigs underwent NGS and bioinformatic analysis (Table S1). A trend toward saturation of distinct peptide sequences relative to the total recovered peptide sequences was found in the tissue samples (Figure 1F; Tables S2 and S3), data consistent with selective homing and enrichment of ligand peptides, and with the non-random distribution observed in previous human screenings.[5,10,16] Certain injured hindleg samples, particularly bone, yielded more distinct sequences relative to the contralateral intact hindleg, indicating that their preferential distribution might represent ligand binding to readily available injury-specific receptors. These results are consistent with the acute molecular and cellular response upon trauma, wherein putative receptors may become accessible to circulating ligands through leakage and/or release via damaged cell membranes.

A large-scale subtractive clustering analysis of the recovered motifs revealed ligand peptide candidates (Table 1) deemed injury-specific (*n* = 23) in soft tissue (*n* = 19) or bone (*n* = 4). To validate the candidacy of this presumed injury-specific ligand subset, a restricted phage panel was generated and re-infused into another injured pig to recover tissues for qPCR-based quantification (Figure 1G). We observed a 27-fold increase in phage particle recovery from the injured hindleg relative to the contralateral intact hindleg within 1–2 h, corroborating the injury-specific homing of the selected panel to the site of trauma (Figure 1H). These candidate ligand peptides were prioritized for validation. Hence, these data suggest that the selected ligand peptides preferentially home to trauma-related receptors. Altogether, this differential homing indicates that certain molecular targets localized in injury sites become readily amenable for biochemical recognition and binding to circulating ligand peptides upon extracellular release and/or protein activation.

Synthetic peptide-affinity purification and identification of candidate receptors

To identify the corresponding receptor(s) for each injury-specific ligand, we integrated multiple methodologies, including synthetic peptide-affinity chromatography, supervised sequence alignment, and *in silico* pathway analysis. Each selected ligand peptide was individually synthesized (*n* = 23; Table 1) and used to purify corresponding candidate receptors from protein extracts of injured or intact control tissues. The purification of candidate receptors was accomplished through peptide-affinity chromatography, gel electrophoresis, and mass spectrometry (Figure S2; Table S4). Candidate receptors (*n* = 82) from various protein classes emerged, with most (59%) being known Ca^{2+} interactors (Figure S3). Specific binding between the ligand peptides and their corresponding candidate receptors was verified by assays on microtiter plates (Figure S4). Two such candidate
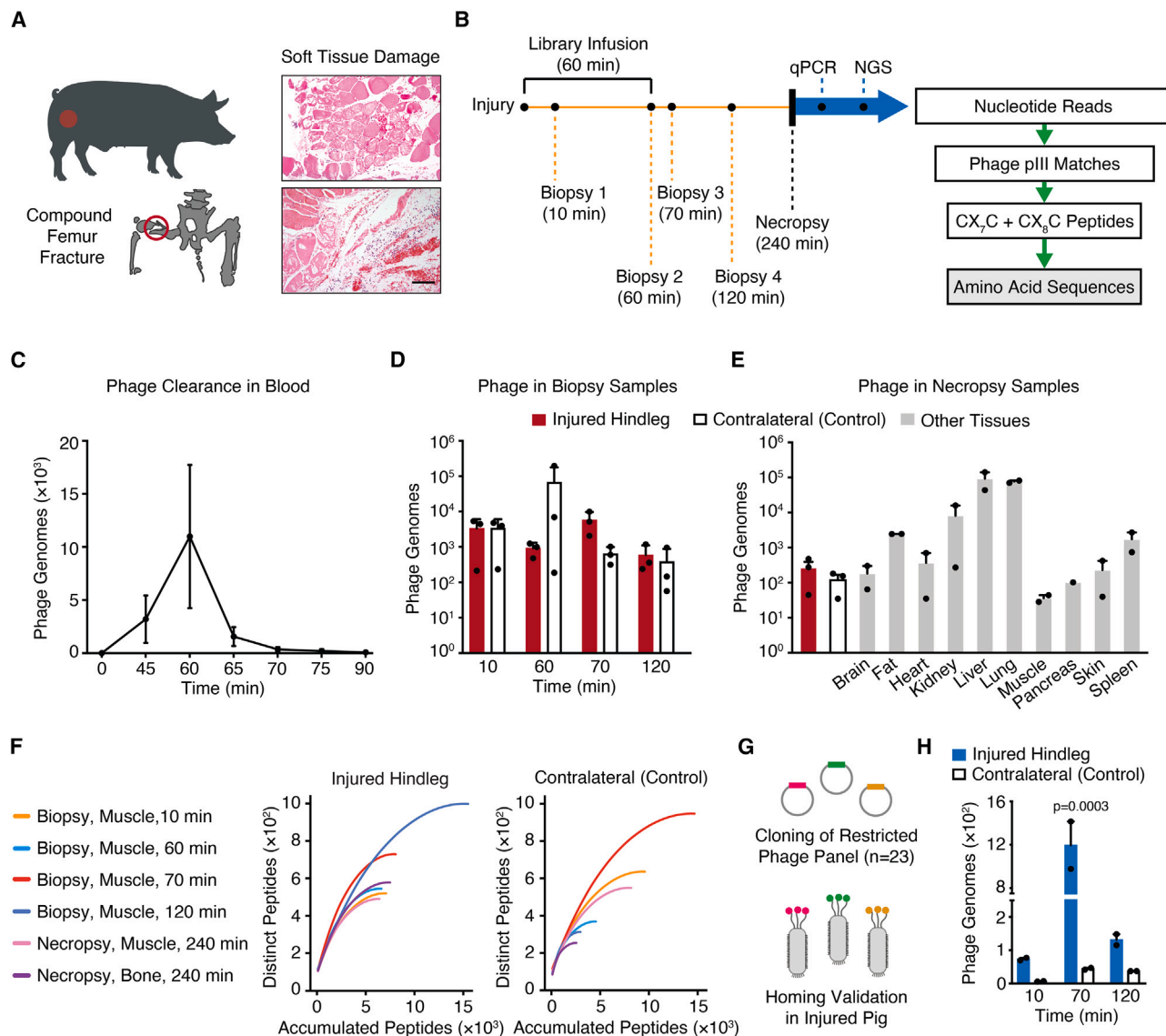
Figure 1. Identification and validation of trauma-specific vascular ligands by combinatorial screening

(A and B) Overview of the *in vivo* phage display peptide library screening and analysis. (A) Utilization of a porcine model of acute trauma involving compound femur fracture and hemorrhagic shock. Representative images of tissue-section biopsies stained with hematoxylin and eosin demonstrate skeletal muscle damage, hemorrhage, infiltration by inflammatory cells, and fibrin accumulation (scale bar, 250 μm). (B) Systemic administration of an *in vivo* phage display peptide library (CX_7C and CX_8C) with sample collection from injured and contralateral intact hindlegs at various time points (10, 60, 70, and 120 min, followed by necropsy at 240 min), followed by evaluation of phage particles per sample.

(C) Profile of phage clearance after systemic phage library infusion in separate injured pigs ($n = 3$) via arterial blood sample collection at different time points by qPCR per 100 ng DNA. Data points corresponding to independent animals (wherein two technical replicates were averaged to obtain a single point) are presented as mean ± standard error of the mean (SEM).

(D) Phage quantification in the injured and contralateral intact hindlegs at fixed biopsy time points by qPCR per 100 ng DNA. Data points corresponding to independent animals (wherein two technical replicates were averaged to obtain a single point) are presented as mean + SEM.

(E) Phage quantification in hindlegs and control organs after necropsy by qPCR per 100 ng DNA. Data points corresponding to independent animals (wherein two technical replicates were averaged to obtain a single point) are presented as mean + SEM.

(F) Saturation plots of distinct peptide sequences in the biopsy and necropsy samples obtained via random shuffling followed by sampling of the recovered peptide sequences that were detected more than once. Data are presented as the mean of 100 rounds of random shuffling/sampling.

(G) Cloning of targeted phage constructs, each displaying a lead peptide candidate ($n = 23$), with their pooling constituting a restricted phage panel.

(H) Administration of the restricted phage panel into a separate injured pig ($n = 1$). Phage were quantified in the injured and contralateral intact hindlegs at various biopsy time points by qPCR per 100 ng DNA. Data points corresponding to technical replicates are presented as mean + SEM and analyzed with two-way ANOVA coupled with *post hoc* Bonferroni's multiple comparisons test.

Table 1. Targeting peptides and their corresponding candidate receptors of the traumome in this study

Peptide no.	Format	Sequence identity	Target tissue[a]	Candidate receptor	Shared with another peptide	Ca2+ interacting[b]	UniProt
1	CX$_8$C	CLRGFPALVC[c]	injured soft tissue	CASQ1	yes; 18	yes	P31415
2	CX$_7$C	CSEIGVRAC	injured soft tissue	HSP27 (HSPB1)	yes; 10	yes	P04792
3	CX$_7$C	CRGFVRGSC[d]	injured soft tissue	CRYAB	yes; 7	yes	P02511
4	CX$_8$C	CSRGSPDARC	injured soft tissue	GC1QBP	no	yes	Q07021
5	CX$_8$C	CSRAKGRGAC	injured soft tissue	DES	yes	no	P17661
6	CX$_7$C	CVLRFFSSC	injured soft tissue	GRP78 (BIP; HSPA5)	no	yes	P11021
7	CX$_8$C	CRPARVRGAC[d]	injured soft tissue	CRYAB	yes; 3	yes	P02511
8	CX$_7$C	CPTFFAVPC	injured soft tissue	CALU	no	yes	O43852
9	CX$_7$C	CASAVPISC	injured soft tissue	PPIB	no	yes	P23284
10	CX$_7$C	CLVSGRSRC	injured soft tissue	HSP27 (HSPB1)	yes; 2	yes	P04792
11	CX$_8$C	CTESFQKHLC	injured soft tissue	PRDX3	no	yes	P30048
12	CX$_8$C	CGILGPWMAC	injured soft tissue	LTF	no	yes	P02788
13	CX$_8$C	CKWEGLDMAC	injured soft tissue	ALDOA	no	yes	P04075
14	CX$_7$C	CLNVSGRSC	injured soft tissue	HSC70 (HSPA8)	no	yes	P11142
15	CX$_8$C	CHKPPNFGSC	injured soft tissue	ANXA1	no	yes	P04083
16	CX$_8$C	CEGKEDMQGC	injured soft tissue	BAG3	no	yes	O95817
17	CX$_8$C	CVGQVGGRRC	injured soft tissue	HRG	no	yes	P04196
18	CX$_7$C	CLRGFQRVC[c]	injured soft tissue	CASQ1	yes; 1	yes	P31415
19	CX$_7$C	CRQRPASGC	injured soft tissue	CALR	no	yes	P27797
20	CX$_8$C	CARASGERGC	fractured bone	COL11A2	no	no	P13942
21	CX$_8$C	CEARASGSRC	fractured bone	CSTA	no	yes	P01040
22	CX$_8$C	CVKASGSRAC	fractured bone	SEC31A	no	yes	O94979
23	CX$_8$C	CVANFGRAPC	fractured bone	CTSG	no	yes	P08311

CLRGFPALVC:CASQ1, CSEIGVRAC:HSP27, and CRQRPASGC:CALR were functionally confirmed. ALDOA, fructose-bisphosphate aldolase A; ANXA1, annexin A1; BAG3, BAG family molecular chaperone regulator 3; BIP, endoplasmic reticulum chaperone BIP; CALR, calreticulin; CALU, calumenin; CASQ1, calsequestrin-1; COL11A2, collagen α-2(XI) chain; CRYAB, α-crystallin B chain; CSTA, cystatin-A; CTSG, cathepsin G; DES, desmin; GC1QBP, complement component 1 Q subcomponent-binding protein (mitochondrial); GRP78, 78-kDa glucose-regulated protein; HRG, histidine-rich glycoprotein; HSC70, heat shock cognate 71-kDa protein; HSP27, heat shock 27-kDa protein; HSPA5, heat shock protein family A (Hsp70) member 5; HSPA8, heat shock protein family A (Hsp70) member 8; LTF, lactotransferrin; PPIB, peptidyl-prolyl *cis*-trans isomerase B; PRDX3, thioredoxin-dependent peroxide reductase (mitochondrial); SEC31A, protein transport protein Sec31A.

[a]Soft tissue includes muscle, fat, fibrous tissue, blood vessels, and/or stromal tissue.
[b]Direct or indirect (i.e., via a single protein mediator).
[c]Contains LRGF motif.
[d]Contains VRG motif.

receptors, calsequestrin-1 (CASQ1) and α-crystallin B chain (CRYAB), were cross-recognized by more than one ligand peptide-targeted phage containing conserved tripeptide motifs such as Leu-Arg-Gly or Val-Arg-Gly (Table 1), thereby supporting guided clustered analysis for the identification of binding motifs with similar biological attributes. Notably, the candidate receptors exhibit sequence conservation across three mammalian proteomes, underscoring their potential significance in the evolutionary context (Table S5).

Ligand-directed targeting of corresponding Ca2+-dependent receptors is specific

Given that Ca2+ is critical for cellular functions,[17] systemic dysregulation of serum Ca2+ levels from tissue injury worsens trauma patient outcomes.[18–21] To investigate the molecular network of Ca2+-dependent receptors in major trauma, we applied Ingenuity Pathway Analysis to map the functional receptor interactions,

with Ca2+ as the central component. Remarkably, the analysis revealed that nearly all non-redundant newly validated receptors (n = 18 out of 20; 90%) interact either directly or indirectly (i.e., through a protein mediator) with Ca2+ (Figure 2A; Table 1). Among the five direct interactors, calreticulin (CALR) was found to be at the center of a large network related to Ca2+ regulation. This interaction map suggests that upon tissue injury, these candidate receptors become targetable by the uncovered ligand peptides in a Ca2+-dependent manner.

To gain functional insights and ascertain ligand-directed binding specificity, three trauma-related peptide-receptor systems (CLRGFPALVC:CASQ1, CSEIGVRAC:HSP27, and CRQRPASGC:CALR) were prioritized for biochemical analysis as representatives of localized targeting of Ca2+-dependent proteins at injury sites. Ligand-receptor interaction specificity was confirmed with binding inhibition assays, wherein increasing concentrations of the cognate synthetic peptides outcompeted peptide-phage binding
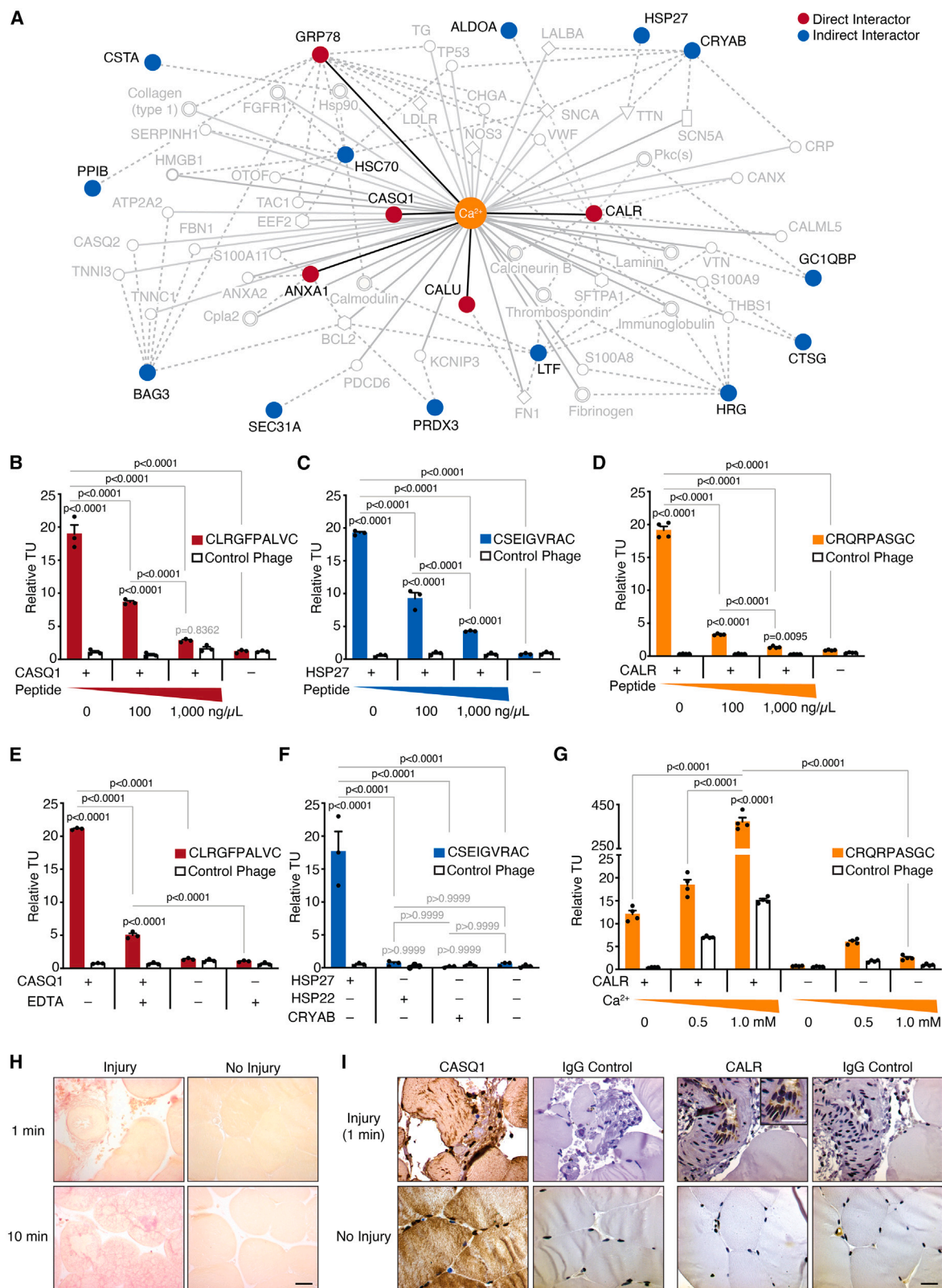
(legend on next page)

to the individual receptors in a concentration-dependent manner (Figures 2B–2D). Notably, specific binding of CLRGFPALVC-displaying phage to immunocaptured CASQ1, the most abundant Ca^{2+}-binding protein in the sarcoplasmic reticulum (SR) of skeletal muscle,[22] was also diminished in the presence of chelating agent 2EDTA, strongly suggesting that Ca^{2+} stabilizes the ligand-receptor interaction (Figure 2E). Ligand-binding specificity of the CSEIGVRAC-displaying phage to HSP27 was also confirmed when tested against two closely related proteins (i.e., HSP22 and CRYAB) of the heat shock protein (HSP) family that act as regulators of cell death (Figure 2F).[23] Like CASQ1, HSP27 organizes muscle fibers at the ultrastructural level[24] and indirectly regulates Ca^{2+} homeostasis.[25] Finally, CRQRPASGC-displaying phage binding to CALR also increased in a Ca^{2+} concentration-dependent manner (Figure 2G). Because CALR shares sequence similarity with CASQ1 and is present in the SR of muscle cells and endoplasmic reticulum (ER) of other cell types,[26] this finding supports its multifunctional role as an intracellular protein with high Ca^{2+}-binding capacity.[27] These results establish that the Ca^{2+}-dependent interaction of three specific ligand-receptor systems localized to injury sites in trauma is specific.

Given the immediate functional role of Ca^{2+} in the context of acute trauma, we evaluated its presence in injured tissue biopsies from serial time points after femur fracture. We detected increased Ca^{2+} levels as early as 1 min post-injury, with a marked rise by 10 min (Figure 2H). In comparison, Ca^{2+} was not detected in the contralateral intact hindleg, reinforcing the selective targetability of Ca^{2+}-dependent receptors in the injured tissue. We subsequently used immunohistochemistry (IHC) to examine two direct Ca^{2+} protein interactors, CASQ1 and CALR, which may have potential for targeted applications. While CASQ1 levels appeared relatively high in the injured hindleg, CASQ1 was also detected in the contralateral intact hindleg, albeit to a lesser degree (Figure 2I, left). However, CALR was exclusively detected in the injured hindleg (Figure 2I, right), rendering it a potentially favorable molecular target. These findings reveal the presence of Ca^{2+} along with the immediate and exclusive targetability of CALR promptly following tissue injury. Thus, we concluded that among all the selected ligand peptides, CRQRPASGC (Table 1, peptide 19) represents an attractive prototype for mechanistic investigation because of its specific binding to cell surface-accessible and/or released CALR from tissue injury in the presence of extracellular Ca^{2+}. Ex vivo overlay assays with tissue samples from the model confirmed the ability of CRQRPASGC-displaying phage to bind to the injured tissues relative to the controls, non-injured tissue samples, and insertless phage (Figure S5A).

Validation of the ligand peptide CRQRPASGC targeting of CALR in major trauma

To confirm the selective peptide targeting of CALR in trauma, we administered CRQRPASGC-displaying or negative control (insertless) phage particles in the porcine model (n = 2 injured pigs per construct). Tissue biopsies from the experiment-injured and contralateral intact hindlegs were collected, and the serial enrichment of phage particles was monitored over time. A gradual increase in CRQRPASGC-displaying phage homing to the injured tissue was observed, peaking at 70 min (Figure 3A), versus control phage (Figure 3B). Homing to the injury site by CRQRPASGC-displaying or control phage was monitored and confirmed with serial IHC (Figure S5B).

Molecular imaging of CRQRPASGC-directed targeting of CALR in tissue injury

Having demonstrated Ca^{2+}-dependent ligand-directed targeting of the injury site, we sought to determine the spatiotemporal attributes of the interaction between the ligand CRQRPASGC and its receptor CALR in injured tissue with molecular imaging. First, we aimed to find which residue(s) of CRQRPASGC would be most critical for its interaction with CALR, with the goal of identifying a

---

Figure 2. Trauma-associated ligand-receptors in the context of Ca^{2+} homeostasis

(A) The traumome, a tentative map of systemically accessible trauma-related proteins. The validated candidate receptors directly (in red) and indirectly (in blue) associated with Ca^{2+} are represented (n = 18 of 20; DES and COL11A2 not shown). Solid lines indicate a direct physical interaction between a protein and Ca^{2+}, and dotted lines indicate a direct physical interaction between two proteins.

(B–D) In vitro phage-binding assays with increasing concentrations of cognate peptide for (B) CLRGFPALVC-displaying phage and immobilized recombinant CASQ1, (C) CSEIGVRAC-displaying phage and immobilized recombinant HSP27, and (D) CRQRPASGC-displaying phage and immobilized recombinant CALR. Phage binding is represented by relative transducing units (TU) as described in STAR Methods. Insertless phage and bovine serum albumin (BSA) served as negative controls for ligand and receptor, respectively. Data points corresponding to technical replicates are presented as mean + SEM and analyzed with three-way ANOVA coupled with post hoc Bonferroni's multiple comparisons test.

(E) Phage-binding in vitro assays with CLRGFPALVC-displaying phage and immobilized immunocaptured CASQ1 in the absence or presence of EDTA (a Ca^{2+} chelator). Phage binding is represented by relative TU as described in STAR Methods. Insertless phage and BSA served as negative controls for ligand and receptor, respectively. Data points corresponding to technical replicates are presented as mean + SEM and analyzed with three-way ANOVA coupled with post hoc Bonferroni's multiple comparisons test.

(F) Phage-binding in vitro assays with CSEIGVRAC-displaying phage and various immobilized heat shock proteins. Phage binding is represented by relative TU as described in STAR Methods. Insertless phage and BSA served as negative controls for ligand and receptor, respectively. Data points corresponding to technical replicates are presented as mean + SEM and analyzed with two-way ANOVA coupled with post hoc Bonferroni's multiple comparisons test.

(G) Phage-binding in vitro assays with increasing concentrations of Ca^{2+} with CRQRPASGC-displaying phage and immobilized recombinant CALR. Phage binding is represented by relative TU as described in STAR Methods. Insertless phage and BSA served as negative controls for ligand and receptor, respectively. Data points corresponding to technical replicates are presented as mean + SEM and analyzed with three-way ANOVA coupled with post hoc Bonferroni's multiple comparisons test.

(H) Immunohistochemical (IHC) staining of Ca^{2+} in muscle tissue-section biopsies from injured and non-injured hindlegs of a porcine model of acute trauma 1 and 10 min after injury (scale bar, 250 μm).

(I) IHC staining of two direct Ca^{2+}-interacting candidate receptors, CASQ1 and CALR, in muscle tissue-section biopsies. Non-injured muscle tissue sections and isotype antibodies were used as negative controls (scale bars, 250 μm).
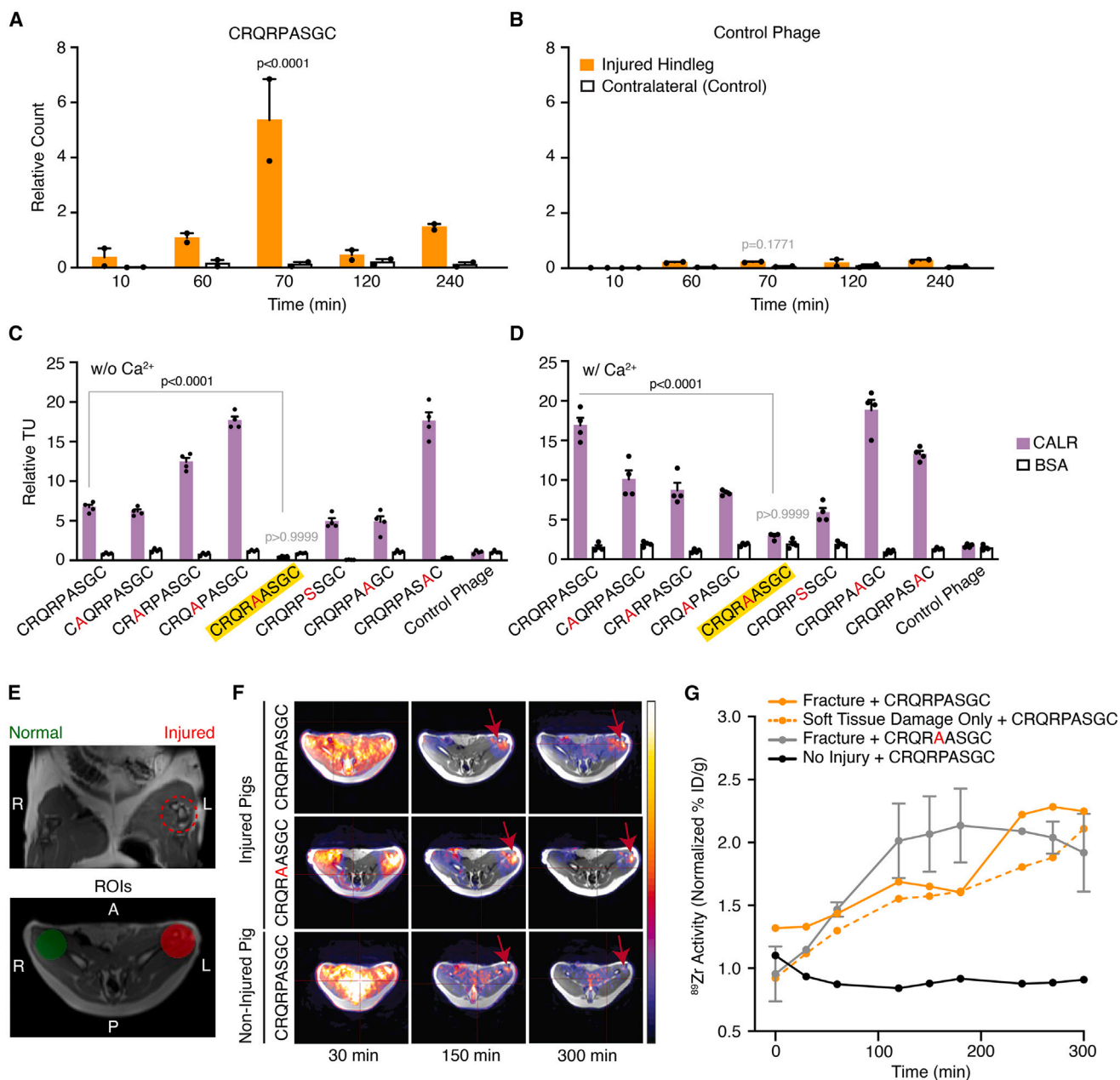
Figure 3. Targeting of the CRQRPASGC-CALR ligand-receptor *in vivo* in the porcine model of major trauma (i.e., femur fracture and/or soft tissue injury) over time

(A and B) Relative homing of (A) CRQRPASGC-displaying or (B) insertless phage to the fractured hindlegs (*n* = 2 pigs each) following administration, assessed by qPCR per 100 ng DNA and normalized to the administered sample. Necropsy was performed at 240 min. The contralateral intact hindleg was used as a negative control. Data points corresponding to independent animals (wherein four technical replicates were averaged to obtain a single point) are presented as mean + SEM and analyzed with two-way ANOVA coupled with *post hoc* Bonferroni's multiple comparisons test.

(C and D) Alanine scanning of CRQRPASGC to assess phage binding of each construct to immobilized recombinant CALR protein in the (C) absence or (D) presence of Ca^{2+}. Each amino acid residue was mutated to an alanine residue except in the instance of an already-present alanine at amino acid position 6, which was mutated to serine. Phage binding is represented by relative TU as described in STAR Methods. Insertless phage and BSA were used as negative controls for ligand and receptor, respectively. Data points corresponding to technical replicates are presented as mean + SEM and analyzed with two-way ANOVA coupled with *post hoc* Bonferroni's multiple comparisons test.

(E) Coronal and axial MRI with regions of interest (ROIs) representing fractured and non-fractured hindlegs of injured pigs for continuous quantification in serial PET/MRI scans.

(legend continued on next page)

mutant with abrogated binding to CALR. We used site-directed alanine scanning to generate mutants for phage-binding assays with immobilized CALR. The mutant P5A peptide (CRQRAASGC) abrogated receptor-binding activity in the absence or presence of Ca^{2+} (Figures 3C and 3D), thereby revealing a critical role of the proline residue in its interaction with CALR. Second, we administered IV ^{89}Zr-labeled CRQRPASGC ($n = 2$ injured pigs and $n = 1$ non-injured pig) or ^{89}Zr-labeled CRQRAASGC ($n = 2$ injured pigs) and performed positron-emission tomography/magnetic resonance imaging (PET/MRI) to serially monitor their temporal dynamics and spatial heterogeneity in injured versus intact control pigs (Figure 3E). PET/MRI scans revealed that ^{89}Zr-CRQRPASGC targets the injured tissue relative to intact tissue (i.e., the contralateral hindleg of the respective injured animal and both hindlegs of the non-injured control animal) as early as 30 min and up to 5 h post-administration (Figure 3F). Quantification of ^{89}Zr-CRQRPASGC-derived radioactivity measured as a percentage of the injected dose per gram in the experiment-injured hindleg relative to the intact control hindleg showed progressive accumulation of ^{89}Zr-CRQRPASGC over 5 h post-administration at the injury site, especially in the femur fracture, and less accumulation in the soft tissue injury without fracture (Figures 3F and 3G). A less prominent initial accumulation of ^{89}Zr-CRQRAASGC at the site of trauma was observed, which may have been due to tissue damage and blood leakage into the injured bone and soft tissues. However, its signal at the injury site continued to increase (comparable to ^{89}Zr-CRQRPASGC) and only reduced by 3 h post-radiotracer administration. Poor perfusion due to edema and vascular spasm at early stages with subsequent improvement of perfusion may explain this latter observation. Alternatively, while CRQRAASGC demonstrated abrogated binding to recombinant CALR *in vitro* under highly stringent experimental conditions (Figures 3C and 3D), it may recognize CALR or perhaps a distinct protein in the *in vivo* microanatomic context at the injury site. Nonetheless, the whole-body images and quantification of ^{89}Zr-CRQRPASGC-derived radioactivity in the contralateral hindleg along with the negative control animal confirmed the lack of non-specific accumulation and its clearance from bone and soft tissue of the extremities in the absence of injury (Figures 3F and 3G).

Despite genomic and proteomic differences across mammalian species, complex tissue microenvironments may resemble one another. To rule out species-specific bias, we selected an independent major trauma model in rats, namely a complete fracture of the femur plus soft tissue damage ($n = 3$) compared to a non-injured control ($n = 1$). We further evaluated the injury-specific targeting capabilities of CRQRPASGC and the binding availability of the CALR receptor by using ^{111}In-DOTA (1,4,7,10-tetraazacyclododecane-1,4,7,10-tetraacetic acid)-CRQRPASGC and single-photon emission computerized tomography combined with conventional computerized tomography (SPECT/CT). Following

hindleg fracture (Figure 4A), ^{111}In-DOTA-CRQRPASGC was administered IV, and scans were serially acquired over 3.5 h. During the initial 18 min, SPECT revealed greater signal from ^{111}In-DOTA-CRQRPASGC in the hindleg with a fractured femur relative to the contralateral intact hindleg and also to the non-injured control rat (Figures 4B–4D, S6A, and S6B). SPECT/CT focused on the hindleg demonstrated high levels of radiolabeled ^{111}In-DOTA-CRQRPASGC-derived radioactivity at the injury site continuously from 1 to 3.5 h, while no radiotracer accumulation was detectable in the contralateral intact hindleg or non-injured control rat (Figure 4E). Time-activity curves confirmed specific accumulation of ^{111}In-DOTA-CRQRPASGC in the injury site (Figures 4F and 4G). The ^{111}In-DOTA-CRQRPASGC-derived radioactivity accumulated in the hindlegs of injured rats was markedly higher than in the non-injured rats at 1 h, with gradual tapering until 3.5 h (Figure 4F). In comparison, ^{111}In-DOTA-CRQRPASGC-derived radioactivity in the intact hindleg(s) of the injured or non-injured control rats was consistently low and exhibited similar kinetics over time (Figure 4G). Measurements corresponding to control organs revealed no specific accumulation of ^{111}In-DOTA-CRQRPASGC. IHC of injured rat tissues confirmed the presence of CALR (Figure S6C). These findings suggest that CRQRPASGC preferentially binds to CALR at the injury site, but not in intact control tissues. Collectively, these independent observations in two different mammalian models of major trauma indicate that CALR promptly (upon Ca^{2+} binding) becomes amenable for specific ligand-directed targeting in injury sites.

Ca^{2+} stabilizes a CALR conformation compatible with ligand peptide binding

We sought to understand the molecular basis for the interaction between CRQRPASGC and CALR in major trauma. Upon soft tissue injury, Ca^{2+} release into the cytoplasmic and/or extracellular microenvironment is rapidly contained by homeostatic autoregulation,[28] such as buffering by Ca^{2+}-binding proteins. Consistent with this pathophysiologic phenomenon, we have demonstrated that CRQRPASGC preferentially homes to injured tissue and binds to CALR in a conditional state of elevated Ca^{2+} concentration. Given that the C terminus of CALR is a highly flexible region predominantly composed of acidic residues with high conformation-stabilizing Ca^{2+}-binding activity and becomes more solvent exposed in the presence of high Ca^{2+} concentrations,[29–31] we surmised that it may encompass the CRQRPASGC-binding region. Hence, we performed peptide-targeted phage-binding assays in the presence of an anti-CALR antibody specifically against its C terminus (residues A353–E416). CRQRPASGC-displaying phage binding was abrogated (Figure 5A), indicating that Ca^{2+} facilitates binding to the C terminus of CALR. Because we have experimentally shown that (1) specific binding of CRQRPASGC to CALR occurs at this region and (2) it increases

(F) Representative serial axial PET/MRI scans of injured pigs administered with ^{89}Zr-labeled CRQRPASGC ($n = 1$ with fracture and $n = 1$ with soft tissue injury only) or ^{89}Zr-labeled mutant peptide (CRQRAASGC; red designates the mutation) ($n = 2$ with fracture) at fixed time points. Each individual image is scaled to the same intensity. ^{89}Zr-labeled CRQRPASGC in a non-injured pig ($n = 1$) was used as a control.

(G) Relative quantification of the ^{89}Zr-labeled peptides at the injured ROI represented as percentage of injected dose per gram normalized to the non-injured ROI (contralateral intact hindleg) over nine time points (0, 30, 60, 120, 150, 180, 240, 270, and 300 min). Data points corresponding to independent animals are presented as either individual values (orange and black lines) or mean ± SEM (gray line).
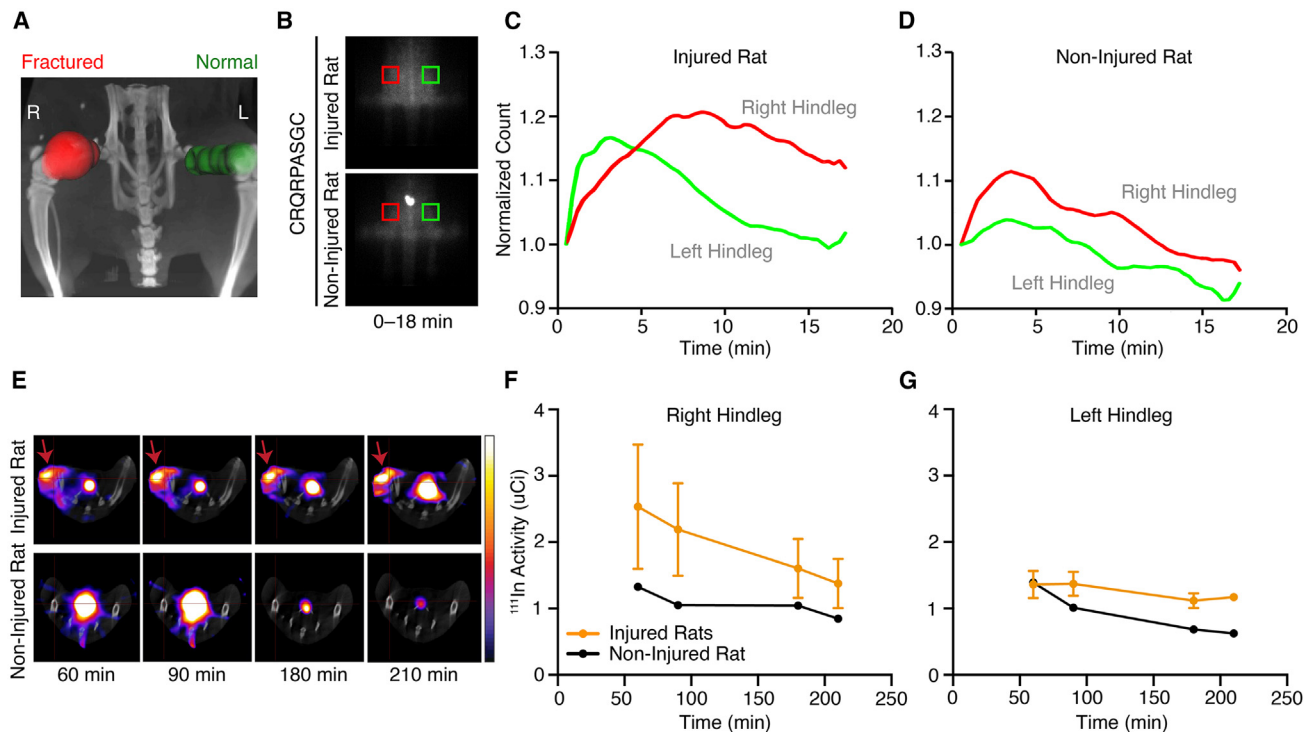
Figure 4. Targeting of the CRQRPASGC-CALR ligand-receptor *in vivo* in a rat model of acute trauma (i.e., femur fracture and soft tissue injury) over time

(A) Coronal CT with ROIs representing fractured (right) and non-fractured (left) hindlegs of injured rats for continuous quantification in serial SPECT/CT scans.

(B) Planar SPECT scan of both hindlegs in a representative injured rat ($n = 1$) and a non-injured rat ($n = 1$) from 0 to 18 min following injection with ^{111}In-DOTA-labeled CRQRPASGC.

(C and D) Quantification of planar SPECT scan from the representative injured rat and non-injured rat. Counts are normalized to the first time point (see Figures S6A and S6B for remaining injured rats).

(E) SPECT/CT scans of the injured rat and non-injured rat at fixed time points (60, 90, 180, and 210 min).

(F and G) Uptake measured at the (F) injured or (G) non-injured hindleg for all rats ($n = 3$ injured rats and $n = 1$ non-injured rat). Data points corresponding to independent animals are presented as either individual values (black line) or mean ± SEM (orange line).

directly with Ca^{2+} concentration, we examined the potential allosteric effects of the peptide-protein interaction on CALR conformation in an injury context-dependent setting; we hypothesized that CRQRPASGC targets a Ca^{2+}-stabilized conformational state of CALR. To model this working hypothesis with steady-state optical methodologies in minimized cell-free assays, we used fluorescence emission spectroscopy to detect changes in CALR conformation upon CRQRPASGC binding, with or without Ca^{2+}; the mutant CRQRAASGC peptide with abrogated *in vitro* binding yet successful *in vivo* homing was also assessed. Steady-state emission spectra of CALR show that CRQRPASGC quenches fluorescence emission of CALR at 280 and 295 nm excitation to a greater degree than the mutant (Figure 5B); moreover, the addition of Ca^{2+} did not affect the emission. Because the observed fluorescence emission quench could be due to nonspecific electrostatic interactions between the positively charged CRQRPASGC or mutant (theoretical isoelectric point [pI] = 9.0 for both peptides) and negatively charged CALR (theoretical pI = 4.3), we further tested this molecular interaction with circular dichroism (CD) spectroscopy. Secondary structural CALR changes were observed upon CRQRPASGC binding (Figure 5C), and to a

lesser degree with the mutant (Figure 5D). An 8-fold increase in peptide concentration demonstrated that CRQRPASGC induced more pronounced secondary structural changes relative to the mutant (Figure 5E). Notably, CALR with Ca^{2+} did not undergo the corresponding structural change when CRQRPASGC was added (Figure 5F). These findings suggest that (1) CRQRPASGC and Ca^{2+} stabilize a specific CALR conformation in a highly similar if not identical manner, and therefore (2) Ca^{2+} binding enables a CALR conformation that is compatible with CRQRPASGC ligand-directed targeting. As shown (Figure 2G), increases in Ca^{2+} concentration facilitate greater binding of CRQRPASGC to CALR, likely precluding binding competition between the two entities. Finally, the mutant peptide weakly binds to and exhibits a similar but less prominent conformational impact on CALR, providing a plausible explanation for its presence in the injured hindlegs of pigs in its previous *in vivo* assessment (Figure 3G).

Peptide-protein structural modeling and molecular dynamics simulation

Having shown a functional interplay among CRQRPASGC, CALR, and Ca^{2+}, we next used *in silico* analysis and peptide
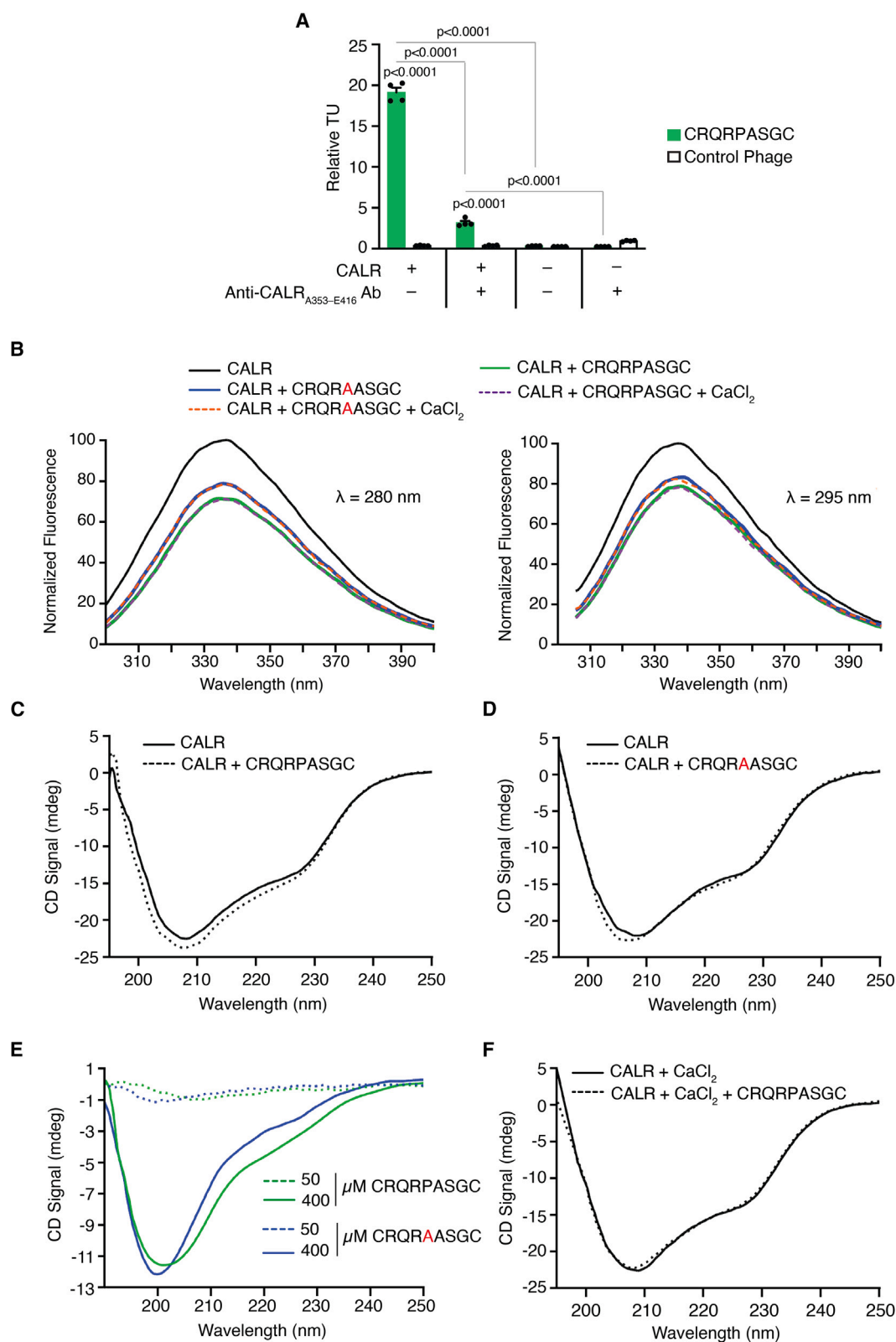
(legend on next page)

structure prediction studies to identify the precise peptide-protein interaction between CRQRPASGC and CALR at the atomic level. We used pathway analysis and sequence alignment to identify CALR interactors with sequence similarities to CRQRPASGC. Among the known direct protein interactors of CALR (n = 67), only four showed partial similarity to CRQRPASGC: tapasin (TAPBP), homeobox protein Nkx-2.1, von Willebrand factor, and myeloperoxidase (Figure S7A). Recent structural characterization of the major histocompatibility complex class I peptide-loading complex revealed that the Pro-Ala-Ser-Gly (PASG) motif (residues D390–E393) of TAPBP (also present in CRQRPASGC) is part of its binding pocket for CALR (at residues E378–E386 of the CALR C terminus; PDB: 6ENY)[32] (Figure 6A). These findings are consistent with the aforementioned inhibition of CRQRPASGC binding to CALR by an anti-CALR antibody (Figure 5A). Finally, we showed that the proline within CRQRPASGC is the most critical residue for binding to CALR (Figures 3C and 3D) and observe that it is highly conserved in TAPBP among mammalian and non-mammalian vertebrate species (Figure S7B), providing additional support for this observation. Additional peptides identified in the injury site from the initial screenings also demonstrate an overlap with this TAPBP region (Figure 6B).

To assess whether the shared PASG motif of CRQRPASGC adopts a similar binding conformation as the corresponding TAPBP region, we performed all-atom explicit-solvent simulations of CRQRPASGC. Low all-atom root-mean-square deviation (RMSD) values (mostly <2 Å) show that the PASG motif within the predicted ligand peptide structure adopts configurations that are highly similar to the native structure of TAPBP (Figures 6C–6E), suggesting a mimicked mode of binding to the CALR C terminus. From a physical perspective, this structural similarity may be attributed to the constraints introduced by cyclization in addition to the specific intramolecular energetic interactions. To structurally assess the role of Ca^{2+} in the conformation-dependent interaction of CALR with CRQRPASGC, we performed all-atom explicit-solvent simulations of CALR with varying Ca^{2+} concentrations. Because we observed that CRQRPASGC binds to the C terminus of CALR, we focused on the last 21 residues of CALR (R366–E386). High RMSD values (>4 Å) were obtained for all Ca^{2+} concentrations relative to the experimental structure (PDB: 6ENY) (Figure 6F). Moreover, the presence of Ca^{2+} reduces the scale of the structural fluctuations of the nine terminal residues of CALR (E378–E386; proposed CRQRPASGC-binding site), where the effect appears more pronounced for negatively charged residues (Figure 6G). This structural analysis indicates that Ca^{2+} binding stabilizes the C

terminus of CALR, which may in turn facilitate CRQRPASGC-directed targeting of injured tissue.

DISCUSSION

Trauma in civilian life and military combat is a substantial and often underrecognized global health issue, accounting for conservative estimates above 4 million deaths annually.[1] Herein, we applied an approach of *in vivo* screenings with a peptide library in a model of femur fracture and hemorrhagic shock[14] integrated with NGS, bioinformatics, and pathway analysis toward the identification of specific functional injury-associated targets. Non-random sequences empirically accumulated in injury samples; among these, we found a panel of ligand peptides and candidate receptors that are evolutionarily conserved and serendipitously interconnected and likely conformationally mediated by Ca^{2+}. We inferred that trauma triggers the sudden dysregulation of Ca^{2+} gradients and exposure to intracellular content.[33,34] To offer a functional working-definition, we have denominated the network of injury-specific receptors that become accessible to the systemic circulation as the traumome; the fast time frame for availability of Ca^{2+}-dependent receptors for ligand-directed targeting (as early as 1 min) endorses immediate molecular target accessibility and/or activation, rather than delayed protein expression.[35] We validated three such ligand-receptor systems for binding specificity and injury-specific accessibility (CLRGFPALVC:CASQ1, CSEIGVRAC:HSP27, and CRQRPASGC:CALR). Furthermore, we described a ligand-directed targeting mechanism of an acquired CALR conformation by CRQRPASGC in the presence of high-levels of Ca^{2+} temporally and spatially released upon tissue injury. Therefore, we show that conformational changes in Ca^{2+}-dependent receptors under major trauma are specifically available to circulating ligands.

Subcellular Ca^{2+} concentrations are tightly regulated with a marked cation gradient between the cytosol (nanomolar range) and specialized organelles such as the SR and ER or extracellular matrix (ECM) compartment (micromolar-to-millimolar range), which is essential for cell physiology.[36] CALR is an intrinsically disordered protein in the cytosol, but it adopts a rigid and compact conformation when Ca^{2+} bound within the ER, SR, or ECM microenvironment.[29,37] As a classical Ca^{2+}-dependent receptor, CALR regulates Ca^{2+} concentration in many processes, including muscular contraction/relaxation.[26,27,38] However, under the unique conditions of unregulated Ca^{2+} overload triggered locally by trauma,[28] the acquired conformational stabilization of CALR provides a plausible rationale for the observed

---

Figure 5. Functional and conformational aspects of the interaction between CRQRPASGC and CALR
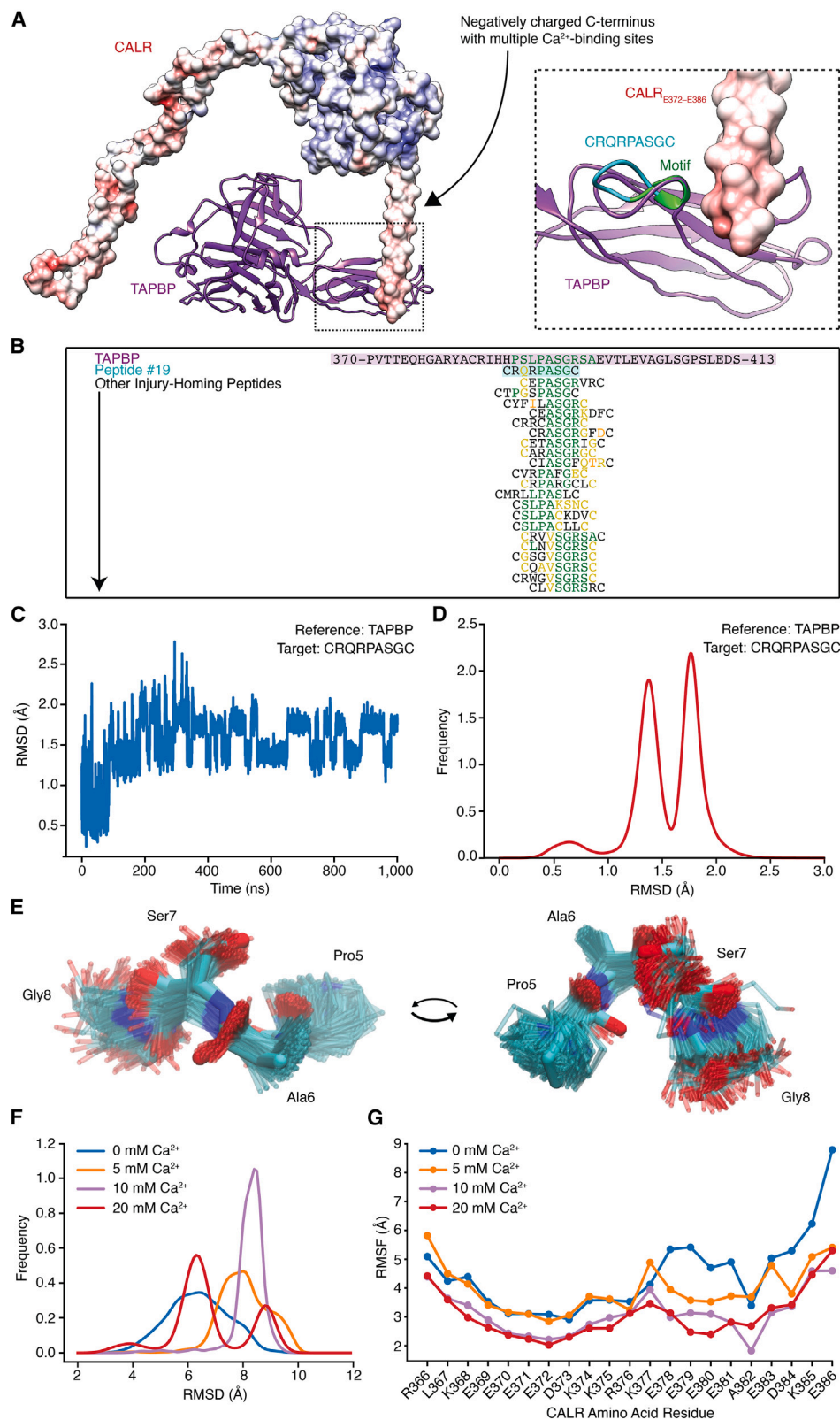
(A) *In vitro* phage-binding assays with CRQRPASGC-displaying phage and immobilized recombinant CALR in the absence or presence of an anti-CALR antibody against its C terminus (residues A353–E416). Data points corresponding to technical replicates are presented as mean ± SEM and analyzed with three-way ANOVA coupled with *post hoc* Bonferroni's multiple comparisons test.

(B) Steady-state fluorescence emission spectra of CALR in the presence of synthetic CRQRPASGC or mutant peptide (CRQRAASGC) in solution with or without $CaCl_2$ under excitation at 280 nm (left) and 295 nm (right).

(C and D) Circular dichroism (CD) spectrum of CALR in the presence of (C) CRQRPASGC (50 μM) or (D) mutant peptide (50 μM).

(E) CD spectra of CALR with a high concentration (400 μM) of CRQRPASGC or mutant peptide subtracted by signal attained with low-concentration peptide (50 μM).

(F) CD spectra of CALR in $CaCl_2$ with or without CRQRPASGC (50 μM) (millidegree is abbreviated to mdeg).

A

CALR

Negatively charged C-terminus
with multiple Ca²⁺-binding sites

TAPBP

CALR$_{E372-E386}$

CRQRPASGC

Motif

TAPBP

B

TAPBP
Peptide #19
Other Injury-Homing Peptides

370-PVTTEQHGARYACRIHHPSLPASGRSAEVTLEVAGLSGPSLEDS-413
CRQRPASGC
CEPASGC
CEPASGRVRC
CTPGSPASGC
CYFILASGRC
CEASGRKDFC
CRRCASGRC
CRASGRGFDC
CETASGRIGC
CARASGRGC
CIASGFQTRC
CVRPAFGEC
CRPARGCLC
CMRLLPASLC
CSLPAKSNC
CSLPACKDVC
CSLPACLLC
CRVVSGRSAC
CLNVSGRSC
CGSGVSGRSC
CQAVSGRSC
CRWGVSGRSRC
CLVSGRSRC

C

Reference: TAPBP
Target: CRQRPASGC

D

Reference: TAPBP
Target: CRQRPASGC

E

Ser7
Gly8
Pro5
Ala6

Ala6
Pro5
Ser7
Gly8

F

0 mM Ca²⁺
5 mM Ca²⁺
10 mM Ca²⁺
20 mM Ca²⁺

G

0 mM Ca²⁺
5 mM Ca²⁺
10 mM Ca²⁺
20 mM Ca²⁺

(legend on next page)

tissue-specific binding of CRQRPASGC. The established role of CALR in wound repair and tissue regeneration further supports its potential as a suitable molecular target in the trauma microenvironment.[39,40] CALR also serves as an "eat me" signal for apoptotic cell clearance during efferocytosis,[41] in which it acts as a cell surface receptor for phagocytes.[42] Hence, it is tempting to conjecture that targeting conformational states of CALR might occur in chronic stress conditions along with acute trauma; we have previously targeted, as experimental precedents, intracellular adapters and stress-response chaperones released into the ECM in cancer[43–46] and an organellar protein in the vascular endothelium serving white adipose tissue in obesity.[8,9]

A few structural and functional aspects deserve comment. We propose the term traumome to designate the set of molecular targets in major trauma, including protein conformations induced by Ca^{2+} binding immediately after injury; conceptually, this network might include allosterically targetable receptors that change conformation upon binding to other divalent cations (e.g., Mg^{2+}, Mn^{2+}, Zn^{2+}), which have distinct concentration gradients among the various intracellular and extracellular compartments. Moreover, additional studies are required to elucidate any downstream signaling processes associated with the traumome. For example, its potential interplay with immune-activating molecules involved in tissue damage, commonly referred to as alarmins and damage-associated molecular patterns,[47–49] currently remains unclear. Next, the initial screenings that serve as the basis for this study were performed in an index non-human large-animal species under controlled conditions. Although specific ligand-receptor interactions were assessed with human proteins, validation of these conceptual and translational findings in humans will be required. Moreover, at least three technical possibilities for the constructs introduced by this original report are noteworthy. For the ligand peptide moiety, peptide-drug conjugates may be developed to counter the time-sensitive sequelae of acute trauma, including (1) coagulation or hemostatic agents for hemorrhage, (2) immunomodulators for inflammation and fat embolism, (3) antibiotics for infection, and (4) angiogenic or bone-regenerating compounds for vascular compromise. For the virus moiety, the peptide-displaying lysogenic phage particles may be adapted as experimental injury-specific antibiotics against multidrug-resistant pathogens if lytic phage particles were used instead.[50–52] For an alternative ligand moiety, the administration of phage display antibody libraries in trauma may enable the identification of injury-targeting antibodies in vivo,[53] which might bestow greater specificity than

peptides. Finally, in addition to compound fractures with shock, whether other types of severe tissue injury (e.g., traumatic brain or spinal cord injury, internal organ damage, extensive burns) have their own conformational receptor subsets remains an open question to be systematically addressed in the appropriate animal models.[54–58]

In summary, we provide initial insight into the collective repertoire of injury-related Ca^{2+}-dependent receptors that become readily available in a spatiotemporal manner for systemic ligand-directed targeting following major trauma. These findings mechanistically underscore the injury-specific conformation-dependent targeting of CALR within the setting of experimental trauma, in which the sudden and immediate exposure of CALR to Ca^{2+} increases its stability for targeting. We also report the discovery and initial functional analysis of CRQRPASGC as a prototype for targeted drug lead optimization and development. The ability of this cyclic nonapeptide to home specifically to injury sites promptly after the traumatic event is central to the concept of the "golden hour" in intensive care for timely therapy delivery to acute trauma patients.[59,60] Given the critical timing for prompt on-site medical attention, future therapeutic applications for emergency use under pre-hospital conditions, such as the systemic administration of a targeted agent to control the sequelae of acute trauma, may be envisioned.

Limitations of the study

Notwithstanding the functional and mechanistic aspects of this study, some inherent limitations must be acknowledged. First, technical aspects associated with the screenings may be adjusted. We performed multiple single-round screenings for the determination of ligand peptides in injured and non-injured tissues as opposed to multi-round, sequential screenings. The advent of NGS has facilitated downstream processing and analysis of DNA sequences encoding ligand peptides displayed on phage in a high-throughput, large-scale manner[16,61,62]; hence, single-round screenings in combination with NGS enable the identification of a large, diverse repertoire of tissue-specific ligand peptides. The classic approach of multi-round screenings wherein phage particles from a tissue of interest are recovered, propagated, and readministered IV into serial organisms, however, has the potential advantage of identifying additional highly selective ligands that may otherwise not be evident with single-round screenings. Second, we validated binding of ligand peptides in vitro to their candidate receptors in their pIII-displayed form, consistent with the screened library format.

Figure 6. In silico structural analysis of CRQRPASGC binding to CALR and the effects of varying concentrations of Ca^{2+} on the proposed binding site

(A) Previously determined structural interaction between TAPBP (purple) and CALR (Coulombic surface coloring where red is negative, blue is positive, and white is neutral) as part of the human peptide-loading complex (PDB: 6ENY). A close-up view of the CALR-binding region (in the C terminus) of TAPBP overlaid with the predicted CRQRPASGC structure (cyan) at the shared PASG motif (green) (interaction details at binding interface cannot be visualized due to the absence of amino acid side-chain resolution).

(B) Sequence alignment of TAPBP with CRQRPASGC and other similar peptides identified in the injury site from the screenings. Identical (green), conserved (orange), and semi-conserved (yellow) amino acid residues are highlighted.

(C and D) (C) All-atom (non-H) RMSD values and (D) their frequencies for the PASG motif of CRQRPASGC across a 1-μs all-atom explicit-solvent simulation relative to the experimental structure of TAPBP.

(E) Overlap of configurations sampled by the PASG motif of CRQRPASGC along the simulation.

(F and G) (F) RMSD value frequencies and (G) per-residue root-mean-square-fluctuation (RMSF) values of simulated C-terminal amino acid residues (R366–E386) of CALR at different Ca^{2+} concentrations (0, 5, 10, and 20 mM) relative to its experimental structure.

Because each phage particle displays 3–5 copies of the DNA-encoded peptide, concerns related to affinity versus avidity are fewer in comparison to other library systems (e.g., pVIII display, wherein each phage particle displays a few hundred peptide copies). Phage-binding assays in which the synthetic peptides outcompeted their corresponding phage-displayed peptides for binding to their candidate receptors support this conclusion. Ongoing and future studies should nonetheless confirm *in vitro* binding of individual synthetic peptides with appropriate readouts (e.g., radiolabeling). Third, the molecular imaging experiments have features that may be improved. Despite its experimental elegance, the P5A mutant of the lead peptide candidate comparatively evaluated was found to have completely abrogated binding to CALR in the *in vitro* phage-binding assays, yet it paradoxically achieved similar levels of homing to the injured pig hindleg and elicited analogous (albeit to a lesser extent) conformational changes in CALR. These findings indicate that P5A might be too stringent to serve as a suitable negative control *in vivo*. Both ligand peptides nonetheless did not localize to the non-injured hindleg, demonstrating trauma-specific homing capabilities attributed to their targeting peptide motif (partially or fully). Alternative peptides, such as scrambled sequences and/or multi-residue mutant versions of CRQRPASGC, may be more appropriate negative controls. Regarding sample composition, the molecular imaging studies were conducted on a relatively small number of animals, all of which were female, as an exploratory quantitative assessment. Additional studies with larger and more heterogeneous cohorts are required for improved characterization of the ligand peptide targeting attributes beyond preclinical settings toward translation into clinical applications.

RESOURCE AVAILABILITY

Lead contact

Requests for further information and resources should be directed to and will be fulfilled by the lead contact, Dr. Renata Pasqualini (renata.pasqualini@rutgers.edu).

Materials availability

All materials and reagents will be made available upon reasonable request and the execution of a material transfer agreement.

Data and code availability

The NGS dataset generated by this study has been deposited into Zenodo (https://doi.org/10.5281/zenodo.14871106). Any additional information required to reanalyze the data reported in this paper is available from the lead contact upon reasonable request.

AUTHOR CONTRIBUTIONS

R.P., J.E.M., C.E.W., J.B.H., and W.A. conceptualized the project. R.P., C.M., D.I.S., A.S.D., E.D.-R., P.C.W., E.M.B., J.K.B., M.C.-V., D.R.C., E.D.-N., W.H.P.D., L.G.-R., S.M., D.N.N., M.G.O., B.P., R.R., T.L.S., G.R.S., F.I.S., F.H.F.T., W.B.B., J.C.S., J.W.B., M.A.D., J.G.G., A.I.B., J.E.M., C.E.W., J.B.H., S.K.B., J.N.O., and W.A. designed the experiments. C.M., D.I.S., A.S.D., E.D-R., E.M.B., J.K.B., M.C-V., D.R.C., E.D-N., W.H.P.D., L.G.-R., S.M., D.N.N., M.G.O., B.P., R.R., T.L.S., G.R.S., F.I.S., F.H.F.T., W.B.B., J.W.B., M.A.D., and A.I.B. performed the experiments. R.P. and W.A. had unrestricted access to all data. R.P., C.M., D.I.S., A.S.D., E.D.-R., P.C.W., E.M.B., J.K.B., M.C.-V., D.R.C., E.D.-N., W.H.P.D., L.G.-R., S.M., D.N.N., F.S.d.O., M.G.O., B.P., R.R., T.L.S., G.R.S., F.I.S., F.H.F.T., W.B.B., J.C.S., J.W.B., M.A.D., J.G.G., A.I.B., J.E.M., C.E.W., J.B.H., S.K.B., J.N.O., and W.A. analyzed and interpreted the data. C.M., A.S.D., and F.S.d.O. performed the statistical analyses. R.P., C.M., D.I.S., A.S.D., E.D.-R., P.C.W., T.L.S., and W.A. wrote the first draft of the manuscript, to which all other authors contributed edits and suggestions. R.P. and W.A. secured major funding and jointly directed the overall project. All authors agreed to submit the manuscript, read and approved the final article, and take responsibility for its content.

DECLARATION OF INTERESTS

R.P. and W.A. are listed as inventors on a provisional patent application related to this technology and would be entitled to standard royalties if commercialization occurs. R.P., J.G.G., and W.A. are founders and equity shareholders of PhageNova Bio. R.P. is the Chief Scientific Officer of and serves as a paid consultant for PhageNova Bio. R.P. and W.A. are founders and equity shareholders of and serve as paid consultants for MBrace Therapeutics. F.I.S. is currently a full-time employee of MBrace Therapeutics. R.P. and W.A. have sponsored research agreements in place with both PhageNova Bio and MBrace Therapeutics. C.E.W. serves as a consultant for CellPhire Therapeutics, is a shareholder of Decisio Health, and receives funding from Grifols and Athersys. J.B.H. serves on the board of directors for Decisio Health, CCJ Medical Devices, QinFlow, Hemostatics, and Zibrio; he is a consultant for the Wake Forest Institute for Regenerative Medicine and Aspen Medical; he receives funding from CSL Behring; he is a co-inventor of the Junctional Emergency Treatment Tool; and he receives royalties from University of Texas (UT) Health. These arrangements are managed in accordance with the established institutional conflict-of-interest policies of the respective institutions. These conflicts of interest fall outside of the scope of this study.

STAR★METHODS

Detailed methods are provided in the online version of this paper and include the following:

- KEY RESOURCES TABLE
- EXPERIMENTAL MODEL AND SUBJECT DETAILS
  - Animals
- METHOD DETAILS
  - Porcine model of compound femur fracture and hemorrhagic shock
  - Phage display library preparation
  - *In vivo* phage display library screenings
  - Bioinformatic analysis of homing peptides
  - Peptide synthesis and radiolabeling
  - Affinity chromatography and phage-binding assays

- ○ *In silico* exploration of relationships between Ca^{2+} and candidate receptors
- ○ Tissue immunohistochemistry
- ○ Homing and molecular imaging of targeted or mutant ligand peptide
- ○ Optical methods: Fluorescence emission spectroscopy and circular dichroism
- ○ CALR interactors and structural modeling of the CRQRPASGC-CALR complex
- ○ Molecular dynamics simulations of CRQRPASGC and CALR
- ● QUANTIFICATION AND STATISTICAL ANALYSIS

SUPPLEMENTAL INFORMATION

Supplemental information can be found online at https://doi.org/10.1016/j.medj.2025.100638.

REFERENCES

1. World Health Organization (2024). Injuries and violence. https://www.who.int/news-room/fact-sheets/detail/injuries-and-violence.

2. Aird, W.C. (2007). Endothelial Biomedicine, 1st Edition (Oxford University Press).

3. Pasqualini, R., and Ruoslahti, E. (1996). Organ targeting in vivo using phage display peptide libraries. Nature *380*, 364–366. https://doi.org/10.1038/380364a0.

4. Arap, W., Pasqualini, R., and Ruoslahti, E. (1998). Cancer treatment by targeted drug delivery to tumor vasculature in a mouse model. Science *279*, 377–380. https://doi.org/10.1126/science.279.5349.377.

5. Arap, W., Kolonin, M.G., Trepel, M., Lahdenranta, J., Cardó-Vila, M., Giordano, R.J., Mintz, P.J., Ardelt, P.U., Yao, V.J., Vidal, C.I., et al. (2002). Steps toward mapping the human vasculature by phage display. Nat. Med. *8*, 121–127. https://doi.org/10.1038/nm0202-121.

6. Staquicini, D.I., Cardó-Vila, M., Rotolo, J.A., Staquicini, F.I., Tang, F.H.F., Smith, T.L., Ganju, A., Schiavone, C., Dogra, P., Wang, Z., et al. (2023). Ceramide as an endothelial cell surface receptor and a lung-specific lipid vascular target for circulating ligands. Proc. Natl. Acad. Sci. USA *120*, e2220269120. https://doi.org/10.1073/pnas.2220269120.

7. Hajitou, A., Trepel, M., Lilley, C.E., Soghomonyan, S., Alauddin, M.M., Marini, F.C., Restel, B.H., Ozawa, M.G., Moya, C.A., Rangel, R., et al. (2006). A hybrid vector for ligand-directed tumor targeting and molecular imaging. Cell *125*, 385–398. https://doi.org/10.1016/j.cell.2006.02.042.

8. Kolonin, M.G., Saha, P.K., Chan, L., Pasqualini, R., and Arap, W. (2004). Reversal of obesity by targeted ablation of adipose tissue. Nat. Med. *10*, 625–632. https://doi.org/10.1038/nm1048.

9. Barnhart, K.F., Christianson, D.R., Hanley, P.W., Driessen, W.H.P., Bernacky, B.J., Baze, W.B., Wen, S., Tian, M., Ma, J., Kolonin, M.G., et al. (2011). A peptidomimetic targeting white fat causes weight loss and improved insulin resistance in obese monkeys. Sci. Transl. Med. *3*, 108ra112. https://doi.org/10.1126/scitranslmed.3002621.

10. Staquicini, F.I., Cardó-Vila, M., Kolonin, M.G., Trepel, M., Edwards, J.K., Nunes, D.N., Sergeeva, A., Efstathiou, E., Sun, J., Almeida, N.F., et al. (2011). Vascular ligand-receptor mapping by direct combinatorial selection in cancer patients. Proc. Natl. Acad. Sci. USA *108*, 18637–18642. https://doi.org/10.1073/pnas.1114503108.

11. Pasqualini, R., Koivunen, E., Kain, R., Lahdenranta, J., Sakamoto, M., Stryhn, A., Ashmun, R.A., Shapiro, L.H., Arap, W., and Ruoslahti, E. (2000). Aminopeptidase N is a receptor for tumor-homing peptides and a target for inhibiting angiogenesis. Cancer Res. *60*, 722–727.

12. Sidman, R.L., Li, J., Lawrence, M., Hu, W., Musso, G.F., Giordano, R.J., Cardó-Vila, M., Pasqualini, R., and Arap, W. (2015). The peptidomimetic vasotide targets two retinal VEGF receptors and reduces pathological angiogenesis in murine and nonhuman primate models of retinal disease. Sci. Transl. Med. *7*, 309ra165. https://doi.org/10.1126/scitranslmed.aac4882.

13. Trepel, M., Arap, W., and Pasqualini, R. (2001). Modulation of the immune response by systemic targeting of antigens to lymph nodes. Cancer Res. *61*, 8110–8112.

14. Cho, S.D., Holcomb, J.B., Tieu, B.H., Englehart, M.S., Morris, M.S., Karahan, Z.A., Underwood, S.A., Muller, P.J., Prince, M.D., Medina, L., et al. (2009). Reproducibility of an animal model simulating complex combat-related injury in a multiple-institution format. Shock *31*, 87–96. https://doi.org/10.1097/SHK.0b013e3181777ffb.

15. Breitwieser, G.E. (2008). Extracellular calcium as an integrator of tissue function. Int. J. Biochem. Cell Biol. *40*, 1467–1480. https://doi.org/10.1016/j.biocel.2008.01.019.

16. Dias-Neto, E., Nunes, D.N., Giordano, R.J., Sun, J., Botz, G.H., Yang, K., Setubal, J.C., Pasqualini, R., and Arap, W. (2009). Next-generation phage display: Integrating and comparing available molecular tools to enable cost-effective high-throughput analysis. PLoS One *4*, e8338. https://doi.org/10.1371/journal.pone.0008338.

17. Carafoli, E., and Krebs, J. (2016). Why calcium? How calcium became the best communicator. J. Biol. Chem. *291*, 20849–20857. https://doi.org/10.1074/jbc.R116.735894.

18. Moore, H.B., Tessmer, M.T., Moore, E.E., Sperry, J.L., Cohen, M.J., Chapman, M.P., Pusateri, A.E., Guyette, F.X., Brown, J.B., Neal, M.D., et al. (2020). Forgot calcium? Admission ionized-calcium in two civilian randomized controlled trials of prehospital plasma for traumatic hemorrhagic shock. J. Trauma Acute Care Surg. *88*, 588–596. https://doi.org/10.1097/TA.0000000000002614.

19. DeBot, M., Sauaia, A., Schaid, T., and Moore, E.E. (2022). Trauma-induced hypocalcemia. Transfusion *62*, S274–S280. https://doi.org/10.1111/trf.16959.

20. Cralley, A.L., Moore, E.E., Coleman, J.R., Vigneshwar, N., Bartley, M., Kissau, D., Eitel, A., Hom, P., Mitra, S., Ghasabyan, A., et al. (2023). Hemorrhagic shock and tissue injury provoke distinct components of trauma-induced coagulopathy in a swine model. Eur. J. Trauma Emerg. Surg. *49*, 1079–1089. https://doi.org/10.1007/s00068-022-02148-x.

21. Kronstedt, S., Roberts, N., Ditzel, R., Elder, J., Steen, A., Thompson, K., Anderson, J., and Siegler, J. (2022). Hypocalcemia as a predictor of mortality and transfusion. A scoping review of hypocalcemia in trauma and hemostatic resuscitation. Transfusion *62*, S158–S166. https://doi.org/10.1111/trf.16965.

22. Rossi, D., Gamberucci, A., Pierantozzi, E., Amato, C., Migliore, L., and Sorrentino, V. (2021). Calsequestrin, a key protein in striated muscle health and disease. J. Muscle Res. Cell Motil. *42*, 267–279. https://doi.org/10.1007/s10974-020-09583-6.

23. Acunzo, J., Katsogiannou, M., and Rocchi, P. (2012). Small heat shock proteins HSP27 (HspB1), alphaB-crystallin (HspB5) and HSP22 (HspB8) as regulators of cell death. Int. J. Biochem. Cell Biol. *44*, 1622–1631. https://doi.org/10.1016/j.biocel.2012.04.002.

24. Kammoun, M., Picard, B., Astruc, T., Gagaoua, M., Aubert, D., Bonnet, M., Blanquet, V., and Cassar-Malek, I. (2016). The invalidation of HspB1 gene in mouse alters the ultrastructural phenotype of muscles. PLoS One *11*, e0158644. https://doi.org/10.1371/journal.pone.0158644.

25. Picard, B., Kammoun, M., Gagaoua, M., Barboiron, C., Meunier, B., Chambon, C., and Cassar-Malek, I. (2016). Calcium homeostasis and muscle energy metabolism are modified in HspB1-null mice. Proteomes *4*, 17. https://doi.org/10.3390/proteomes4020017.

26. Smith, M.J., and Koch, G.L. (1989). Multiple zones in the sequence of calreticulin (CRP55, calregulin, HACBP), a major calcium binding ER/SR protein. EMBO J. *8*, 3581–3586. https://doi.org/10.1002/j.1460-2075.1989.tb08530.x.

27. Michalak, M., Corbett, E.F., Mesaeli, N., Nakamura, K., and Opas, M. (1999). Calreticulin: one protein, one gene, many functions. Biochem. J. *344*, 281–292.

28. Gissel, H. (2005). The role of Ca2+ in muscle cell damage. Ann. N. Y. Acad. Sci. *1066*, 166–180. https://doi.org/10.1196/annals.1363.013.

29. Villamil Giraldo, A.M., Lopez Medus, M., Gonzalez Lebrero, M., Pagano, R.S., Labriola, C.A., Landolfo, L., Delfino, J.M., Parodi, A.J., and Caramelo, J.J. (2010). The structure of calreticulin C-terminal domain is modulated by physiological variations of calcium concentration. J. Biol. Chem. *285*, 4544–4553. https://doi.org/10.1074/jbc.M109.034512.

30. Li, Z., Stafford, W.F., and Bouvier, M. (2001). The metal ion binding properties of calreticulin modulate its conformational flexibility and thermal stability. Biochemistry *40*, 11193–11201. https://doi.org/10.1021/bi010948l.

31. Wijeyesakere, S.J., Gafni, A.A., and Raghavan, M. (2011). Calreticulin is a thermostable protein with distinct structural responses to different divalent cation environments. J. Biol. Chem. *286*, 8771–8785. https://doi.org/10.1074/jbc.M110.169193.

32. Blees, A., Januliene, D., Hofmann, T., Koller, N., Schmidt, C., Trowitzsch, S., Moeller, A., and Tampé, R. (2017). Structure of the human MHC-I peptide-loading complex. Nature *551*, 525–528. https://doi.org/10.1038/nature24627.

33. Moriscot, A., Miyabara, E.H., Langeani, B., Belli, A., Egginton, S., and Bowen, T.S. (2021). Firearms-related skeletal muscle trauma: Pathophysiology and novel approaches for regeneration. NPJ Regen. Med. *6*, 17. https://doi.org/10.1038/s41536-021-00127-1.

34. Cho, C.H., Woo, J.S., Perez, C.F., and Lee, E.H. (2017). A focus on extracellular Ca(2+) entry into skeletal muscle. Exp. Mol. Med. *49*, e378. https://doi.org/10.1038/emm.2017.208.

35. Ozawa, M.G., Zurita, A.J., Dias-Neto, E., Nunes, D.N., Sidman, R.L., Gelovani, J.G., Arap, W., and Pasqualini, R. (2008). Beyond receptor expression levels: the relevance of target accessibility in ligand-directed pharmacodelivery systems. Trends Cardiovasc. Med. *18*, 126–132. https://doi.org/10.1016/j.tcm.2008.03.001.

36. Kuo, I.Y., and Ehrlich, B.E. (2015). Signaling in muscle contraction. Cold Spring Harbor Perspect. Biol. *7*, a006023. https://doi.org/10.1101/cshperspect.a006023.

37. Migliaccio, A.R., and Uversky, V.N. (2018). Dissecting physical structure of calreticulin, an intrinsically disordered Ca(2+)-buffering chaperone from endoplasmic reticulum. J. Biomol. Struct. Dyn. *36*, 1617–1636. https://doi.org/10.1080/07391102.2017.1330224.

38. Ostwald, T.J., and MacLennan, D.H. (1974). Isolation of a high affinity calcium-binding protein from sarcoplasmic reticulum. J. Biol. Chem. *249*, 974–979.

39. Nanney, L.B., Woodrell, C.D., Greives, M.R., Cardwell, N.L., Pollins, A.C., Bancroft, T.A., Chesser, A., Michalak, M., Rahman, M., Siebert, J.W., and Gold, L.I. (2008). Calreticulin enhances porcine wound repair by diverse biological effects. Am. J. Pathol. *173*, 610–630. https://doi.org/10.2353/ajpath.2008.071027.

40. Stack, M.E., Mishra, S., Parimala Chelvi Ratnamani, M., Wang, H., Gold, L.I., and Wang, H. (2022). Biomimetic extracellular matrix nanofibers electrospun with calreticulin promote synergistic activity for tissue regeneration. ACS Appl. Mater. Interfaces *14*, 51683–51696. https://doi.org/10.1021/acsami.2c13887.

41. Gold, L.I., Rahman, M., Blechman, K.M., Greives, M.R., Churgin, S., Michaels, J., Callaghan, M.J., Cardwell, N.L., Pollins, A.C., Michalak, M., et al. (2006). Overview of the role for calreticulin in the enhancement of wound healing through multiple biological effects. J. Invest. Dermatol. Symp. Proc. *11*, 57–65. https://doi.org/10.1038/sj.jidsymp.5650011.

42. Gardai, S.J., McPhillips, K.A., Frasch, S.C., Janssen, W.J., Starefeldt, A., Murphy-Ullrich, J.E., Bratton, D.L., Oldenborg, P.A., Michalak, M., and Henson, P.M. (2005). Cell-surface calreticulin initiates clearance of viable or apoptotic cells through trans-activation of LRP on the phagocyte. Cell *123*, 321–334. https://doi.org/10.1016/j.cell.2005.08.032.

43. Mintz, P.J., Cardó-Vila, M., Ozawa, M.G., Hajitou, A., Rangel, R., Guzman-Rojas, L., Christianson, D.R., Arap, M.A., Giordano, R.J., Souza, G.R., et al. (2009). An unrecognized extracellular function for an intracellular adapter protein released from the cytoplasm into the tumor microenvironment. Proc. Natl. Acad. Sci. USA *106*, 2182–2187. https://doi.org/10.1073/pnas.0807543105.

44. Vidal, C.I., Mintz, P.J., Lu, K., Ellis, L.M., Manenti, L., Giavazzi, R., Gershenson, D.M., Broaddus, R., Liu, J., Arap, W., and Pasqualini, R. (2004). An HSP90-mimic peptide revealed by fingerprinting the pool of antibodies from ovarian cancer patients. Oncogene *23*, 8859–8867. https://doi.org/10.1038/sj.onc.1208082.

45. Mintz, P.J., Kim, J., Do, K.A., Wang, X., Zinner, R.G., Cristofanilli, M., Arap, M.A., Hong, W.K., Troncoso, P., Logothetis, C.J., et al. (2003). Fingerprinting the circulating repertoire of antibodies from cancer patients. Nat. Biotechnol. *21*, 57–63. https://doi.org/10.1038/nbt774.

46. Arap, M.A., Lahdenranta, J., Mintz, P.J., Hajitou, A., Sarkis, A.S., Arap, W., and Pasqualini, R. (2004). Cell surface expression of the stress response chaperone GRP78 enables tumor targeting by circulating ligands. Cancer Cell *6*, 275–284. https://doi.org/10.1016/j.ccr.2004.08.018.

47. Manson, J., Thiemermann, C., and Brohi, K. (2012). Trauma alarmins as activators of damage-induced inflammation. Br. J. Surg. *99*, 12–20. https://doi.org/10.1002/bjs.7717.

48. Chan, J.K., Roth, J., Oppenheim, J.J., Tracey, K.J., Vogl, T., Feldmann, M., Horwood, N., and Nanchahal, J. (2012). Alarmins: Awaiting a clinical response. J. Clin. Investig. *122*, 2711–2719. https://doi.org/10.1172/JCI62423.

49. Relja, B., and Land, W.G. (2020). Damage-associated molecular patterns in trauma. Eur. J. Trauma Emerg. Surg. *46*, 751–775. https://doi.org/10.1007/s00068-019-01235-w.

50. Gelman, D., Eisenkraft, A., Chanishvili, N., Nachman, D., Coppenhagem Glazer, S., and Hazan, R. (2018). The history and promising future of phage therapy in the military service. J. Trauma Acute Care Surg. *85*, S18–S26. https://doi.org/10.1097/TA.0000000000001809.

51. Eskenazi, A., Lood, C., Wubbolts, J., Hites, M., Balarjishvili, N., Leshkasheli, L., Askilashvili, L., Kvachadze, L., van Noort, V., Wagemans, J., et al. (2022). Combination of pre-adapted bacteriophage therapy and antibiotics for treatment of fracture-related infection due to pandrug-resistant Klebsiella pneumoniae. Nat. Commun. *13*, 302. https://doi.org/10.1038/s41467-021-27656-z.

52. Uyttebroek, S., Chen, B., Onsea, J., Ruythooren, F., Debaveye, Y., Devolder, D., Spriet, I., Depypere, M., Wagemans, J., Lavigne, R., et al. (2022). Safety and efficacy of phage therapy in difficult-to-treat infections: A systematic review. Lancet Infect. Dis. *22*, e208–e220. https://doi.org/10.1016/S1473-3099(21)00612-5.

53. D'Angelo, S., Staquicini, F.I., Ferrara, F., Staquicini, D.I., Sharma, G., Tarleton, C.A., Nguyen, H., Naranjo, L.A., Sidman, R.L., Arap, W., et al. (2018). Selection of phage-displayed accessible recombinant targeted antibodies (SPARTA): methodology and applications. JCI Insight *3*, e98305. https://doi.org/10.1172/jci.insight.98305.

54. Mann, A.P., Scodeller, P., Hussain, S., Joo, J., Kwon, E., Braun, G.B., Mölder, T., She, Z.G., Kotamraju, V.R., Ranscht, B., et al. (2016). A peptide for targeted, systemic delivery of imaging and therapeutic compounds into acute brain injuries. Nat. Commun. *7*, 11980. https://doi.org/10.1038/ncomms11980.

55. Martinez, B.I., Mousa, G.A., Fleck, K., MacCulloch, T., Diehnelt, C.W., Stephanopoulos, N., and Stabenfeldt, S.E. (2022). Uncovering temporospatial sensitive TBI targeting strategies via in vivo phage display. Sci. Adv. *8*, eabo5047. https://doi.org/10.1126/sciadv.abo5047.

56. Palmers, I., Ydens, E., Put, E., Depreitere, B., Bongers-Janssen, H., Pickkers, P., Hendrix, S., and Somers, V. (2016). Antibody profiling identifies novel antigenic targets in spinal cord injury patients. J. Neuroinflammation *13*, 243. https://doi.org/10.1186/s12974-016-0713-5.

57. Costantini, T.W., Eliceiri, B.P., Putnam, J.G., Bansal, V., Baird, A., and Coimbra, R. (2012). Intravenous phage display identifies peptide

sequences that target the burn-injured intestine. Peptides *38*, 94–99. https://doi.org/10.1016/j.peptides.2012.08.015.

58. Järvinen, T.A.H., and Ruoslahti, E. (2007). Molecular changes in the vasculature of injured tissues. Am. J. Pathol. *171*, 702–711. https://doi.org/10.2353/ajpath.2007.061251.

59. Kotwal, R.S., Howard, J.T., Orman, J.A., Tarpey, B.W., Bailey, J.A., Champion, H.R., Mabry, R.L., Holcomb, J.B., and Gross, K.R. (2016). The effect of a golden hour policy on the morbidity and mortality of combat casualties. JAMA Surg. *151*, 15–24. https://doi.org/10.1001/jamasurg.2015.3104.

60. Moore, E.E., Moore, H.B., Kornblith, L.Z., Neal, M.D., Hoffman, M., Mutch, N.J., Schöchl, H., Hunt, B.J., and Sauaia, A. (2021). Trauma-induced coagulopathy. Nat. Rev. Dis. Primers *7*, 30. https://doi.org/10.1038/s41572-021-00264-3.

61. Pleiko, K., Põšnograjeva, K., Haugas, M., Paiste, P., Tobi, A., Kurm, K., Riekstina, U., and Teesalu, T. (2021). In vivo phage display: Identification of organ-specific peptides using deep sequencing and differential profiling across tissues. Nucleic Acids Res. *49*, e38. https://doi.org/10.1093/nar/gkaa1279.

62. Ivanova, A., Kohl, F., González-King Garibotti, H., Chalupska, R., Cvjetkovic, A., Firth, M., Jennbacken, K., Martinsson, S., Silva, A.M., Viken, I., et al. (2024). In vivo phage display identifies novel peptides for cardiac targeting. Sci. Rep. *14*, 12177. https://doi.org/10.1038/s41598-024-62953-9.

63. Smith, G.P. (2024). Principles of affinity selection. Cold Spring Harb. Protoc. *2024*. https://doi.org/10.1101/pdb.over107894.

64. Barbas, I.I.I.,C.F., Burton, D.R., Scott, J.K., and Silverman, G.J. (2001). Phage Display: A Laboratory Manual (Cold Spring Harbor Laboratory Press).

65. R Core Team (2021). R: A Language and Environment for Statistical Computing (R Foundation for Statistical Computing).

66. Thomas, P.D., Ebert, D., Muruganujan, A., Mushayahama, T., Albou, L.P., and Mi, H. (2022). PANTHER: making genome-scale phylogenetics accessible to all. Protein Sci. *31*, 8–22. https://doi.org/10.1002/pro.4218.

67. Kramer, A., Green, J., Pollard, J., Jr., and Tugendreich, S. (2014). Causal analysis approaches in Ingenuity Pathway Analysis. Bioinformatics *30*, 523–530. https://doi.org/10.1093/bioinformatics/btt703.

68. Staquicini, D.I., Barbu, E.M., Zemans, R.L., Dray, B.K., Staquicini, F.I., Dogra, P., Cardó-Vila, M., Miranti, C.K., Baze, W.B., Villa, L.L., et al. (2021). Targeted phage display-based pulmonary vaccination in mice and non-human primates. Médica Sur *2*, 321–342. https://doi.org/10.1016/j.medj.2020.10.005.

69. Bronk, J.K., Russell, B.H., Rivera, J.J., Pasquali, R., Arap, W., Höök, M., and Barbu, E.M. (2014). A multifunctional streptococcal collagen-mimetic protein coating prevents bacterial adhesion and promotes osteoid formation on titanium. Acta Biomater. *10*, 3354–3362. https://doi.org/10.1016/j.actbio.2014.04.005.

70. Shen, Y., Maupetit, J., Derreumaux, P., and Tufféry, P. (2014). Improved PEP-FOLD approach for peptide and miniprotein structure prediction.

71. Pettersen, E.F., Goddard, T.D., Huang, C.C., Couch, G.S., Greenblatt, D.M., Meng, E.C., and Ferrin, T.E. (2004). UCSF Chimera–A visualization system for exploratory research and analysis. J. Comput. Chem. *25*, 1605–1612. https://doi.org/10.1002/jcc.20084.

72. Markosian, C., Staquicini, D.I., Dogra, P., Dodero-Rojas, E., Lubin, J.H., Tang, F.H.F., Smith, T.L., Contessoto, V.G., Libutti, S.K., Wang, Z., et al. (2022). Genetic and structural analysis of SARS-CoV-2 spike protein for universal epitope selection. Mol. Biol. Evol. *39*, msac091. https://doi.org/10.1093/molbev/msac091.

73. Staquicini, D.I., Tang, F.H.F., Markosian, C., Yao, V.J., Staquicini, F.I., Dodero-Rojas, E., Contessoto, V.G., Davis, D., O'Brien, P., Habib, N., et al. (2021). Design and proof of concept for targeted phage-based COVID-19 vaccination strategies with a streamlined cold-free supply chain. Proc. Natl. Acad. Sci. USA *118*, e2105739118. https://doi.org/10.1073/pnas.2105739118.

74. Hess, B., Kutzner, C., van der Spoel, D., and Lindahl, E. (2008). GROMACS 4: Algorithms for highly efficient, load-balanced, and scalable molecular simulation. J. Chem. Theor. Comput. *4*, 435–447. https://doi.org/10.1021/ct700301q.

75. Lindahl, E., Hess, B., and van der Spoel, D. (2001). GROMACS 3.0: A package for molecular simulation and trajectory analysis. J. Mol. Model. *7*, 306–317. https://doi.org/10.1007/s008940100045.

76. Lindorff-Larsen, K., Piana, S., Palmo, K., Maragakis, P., Klepeis, J.L., Dror, R.O., and Shaw, D.E. (2010). Improved side-chain torsion potentials for the Amber ff99SB protein force field. Proteins *78*, 1950–1958. https://doi.org/10.1002/prot.22711.

77. Jorgensen, W.L., Chandrasekhar, J., Madura, J.D., Impey, R.W., and Klein, M.L. (1983). Comparison of simple potential functions for simulating liquid water. J. Chem. Phys. *79*, 926–935. https://doi.org/10.1063/1.445869.

78. Parrinello, M., and Rahman, A. (1981). Polymorphic transitions in single crystals: A new molecular dynamics method. J. Appl. Phys. *52*, 7182–7190. https://doi.org/10.1063/1.328693.

79. Hoover, W.G. (1985). Canonical dynamics: Equilibrium phase-space distributions. Phys. Rev. A Gen. Phys. *31*, 1695–1697. https://doi.org/10.1103/physreva.31.1695.

80. Nosé, S. (1984). A unified formulation of the constant temperature molecular dynamics methods. J. Chem. Phys. *81*, 511–519. https://doi.org/10.1063/1.447334.

81. Eastman, P., Swails, J., Chodera, J.D., McGibbon, R.T., Zhao, Y., Beauchamp, K.A., Wang, L.P., Simmonett, A.C., Harrigan, M.P., Stern, C.D., et al. (2017). OpenMM 7: Rapid development of high performance algorithms for molecular dynamics. PLoS Comput. Biol. *13*, e1005659. https://doi.org/10.1371/journal.pcbi.1005659.

82. Fox, J. (2005). The R Commander: A basic statistics graphical user interface to R. J. Stat. Software *14*, 1–42.

83. Fox, J., and Bouchet-Valat, M. (2020). Rcmdr: R Commander. R package version *2*, 7.

(continued top of left column) J. Chem. Theor. Comput. *10*, 4745–4758. https://doi.org/10.1021/ct500592m.

STAR★METHODS

KEY RESOURCES TABLE

REAGENT or RESOURCE	SOURCE	IDENTIFIER
Antibodies		
Anti-fd bacteriophage antibody	Sigma-Aldrich	Cat#B7786
anti-CASQ antibody	Invitrogen	Cat#MA3-913
Anti-CASQ1/2 antibody	Abcam	Cat#ab3516
anti-CALR antibody	Abcam	Cat#ab14234
Anti-rabbit horseradish peroxidase (HRP)-conjugated secondary antibody	Jackson ImmunoResearch	Cat#111-035-003
Anti-chicken horseradish peroxidase (HRP)-conjugated secondary antibody	Jackson ImmunoResearch	Cat#703-035-155
Bacterial and viral strains		
fUSE5 bacteriophage vector	Laboratory of Dr. George P. Smith	N/A
Phage display peptide libraries (CX_7C and CX_8C)	Laboratory of Dr. Renata Pasqualini and Dr. Wadih Arap	N/A
K91 *E. coli*	Laboratory of Dr. George P. Smith	N/A
MC1061 competent *E.coli*	Laboratory of Dr. Renata Pasqualini and Dr. Wadih Arap	N/A
ElectroMAX DH5α-E competent cells	Invitrogen	Cat#11319019
Biological samples		
Sus scrofa domesticus tissues	Sinclair Bio Resources	N/A
Rattus norvegicus tissues	MPI Research	N/A
Chemicals, peptides, and recombinant proteins		
Bovine serum albumin	Sigma-Aldrich	Cat#A4737
Luria Broth with agar	Sigma-Aldrich	Cat#L3147
BcMag long-arm amine-terminated magnetic beads	Bioclone	Cat#FA-115
SYPRO Ruby Protein Gel Stain	Invitrogen	Cat#S12000
Ethylenediaminetetraacetic acid (EDTA)	Invitrogen	Cat#AM9260G
$CaCl_2$	Sigma-Aldrich	Cat#10043-52-4
CLRGFPALVC peptide (C_1-C_{10} disulfide bridge)	CPC Scientific	N/A
CSEIGVRAC peptide (C_1-C_9 disulfide bridge)	CPC Scientific	N/A
CRGFVRGSC peptide (C_1-C_9 disulfide bridge)	CPC Scientific	N/A
CSRGSPDARC peptide (C_1-C_{10} disulfide bridge)	CPC Scientific	N/A
CSRAKGRGAC peptide (C_1-C_{10} disulfide bridge)	CPC Scientific	N/A
CVLRFFSSC peptide (C_1-C_9 disulfide bridge)	CPC Scientific	N/A
CRPARVRGAC peptide (C_1-C_{10} disulfide bridge)	CPC Scientific	N/A
CPTFFAVPC peptide (C_1-C_9 disulfide bridge)	CPC Scientific	N/A
CASAVPISC peptide (C_1-C_9 disulfide bridge)	CPC Scientific	N/A
CLVSGRSRC peptide (C_1-C_9 disulfide bridge)	CPC Scientific	N/A
CTESFQKHLC peptide (C_1-C_{10} disulfide bridge)	CPC Scientific	N/A
CGILGPWMAC peptide (C_1-C_{10} disulfide bridge)	CPC Scientific	N/A
CKWEGLDMAC peptide (C_1-C_{10} disulfide bridge)	CPC Scientific	N/A
CLNVSGRSC peptide (C_1-C_9 disulfide bridge)	CPC Scientific	N/A
CHKPPNFGSC peptide (C_1-C_{10} disulfide bridge)	CPC Scientific	N/A
CEGKEDMQGC peptide (C_1-C_{10} disulfide bridge)	CPC Scientific	N/A
CVGQVGGRRC peptide (C_1-C_{10} disulfide bridge)	CPC Scientific	N/A
CLRGFQRVC peptide (C_1-C_9 disulfide bridge)	CPC Scientific	N/A

(*Continued on next page*)

Continued

REAGENT or RESOURCE	SOURCE	IDENTIFIER
CRQRPASGC peptide (C_1-C_9 disulfide bridge)	CPC Scientific	N/A
CARASGERGC peptide (C_1-C_{10} disulfide bridge)	CPC Scientific	N/A
CEARASGSRC peptide (C_1-C_{10} disulfide bridge)	CPC Scientific	N/A
CVKASGSRAC peptide (C_1-C_{10} disulfide bridge)	CPC Scientific	N/A
CVANFGRAPC peptide (C_1-C_{10} disulfide bridge)	CPC Scientific	N/A
DFO-KK-PEG2-CRQRPASGC-PEG2-KK (C_1-C_9 disulfide bridge)	CPC Scientific	N/A
DFO-KK-PEG2-CRQRAASGC-PEG2-KK (C_1-C_9 disulfide bridge)	CPC Scientific	N/A
NH_2-Cys-KK-PEG2-CRQRPASGC-PEG2-KK-COOH (C_1-C_9 disulfide bridge)	CPC Scientific	N/A
^{89}Zr	3D Imaging LLC	N/A
^{111}In	MPI Research	N/A
CALR, human recombinant protein	OriGene / Abnova	Cat#TP303222 / Cat#H00000811-P01
CASQ1, human recombinant protein	Abnova	Cat#H00000844-P01
HSP27, human recombinant protein	ATGen	Cat#ATGP0444
HSP22, human recombinant protein	bioWORLD	Cat#22060349-1
CRYAB, human recombinant protein	Abcam	Cat#ab48779
Dual Endogenous Enzyme-Blocking Reagent	Agilent Dako	Cat#S200389-2
Protein Block	Agilent Dako	Cat#X090930-2
Alizarin Red S	Sigma-Aldrich	Cat#A5533
Polyethylene glycol (PEG) 8000	Thermo Scientific Chemicals	Cat#043443-A3
Triton X-114	Sigma-Aldrich	Cat#9036-19-5
Critical commercial assays		
DNeasy Blood and Tissue Kit	QIAGEN	Cat#69504
Plasmid Plus Giga Kit	QIAGEN	Cat#12991
QIAquick PCR Purification Kit	QIAGEN	Cat#28106
QIAquick Nucleotide Removal Kit	QIAGEN	Cat#28306
QIAprep Spin Miniprep Kit	QIAGEN	Cat#27104
Sequenase DNA polymerase	Amersham	Cat#70770
Kinetic-QCL Kinetic Chromogenic LAL Assay	Lonza Bioscience	Cat#50-650U
Pierce BCA Protein Assay Kit	Thermo Scientific	Cat#23227
Experimental models: Organisms/strains		
Sinclair miniature pigs (*Sus scrofa domesticus*)	Sinclair Bio Resources	N/A
Sprague-Dawley rats (*Rattus norvegicus*)	MPI Research	N/A
Oligonucleotides		
fUSE5 forward primer: 5′-TGAGGTGGTATCGGCAATGA-3′	Sigma-Aldrich	N/A
fUSE5 reverse primer: 5′-GGATGCTGTATTTAGGCCGTTT-3′	Sigma-Aldrich	N/A
NGS forward primer: 5′-CGCAATTCCTTTAGTTGTTCC-3′	Sigma-Aldrich	N/A
NGS reverse primer: 5′-TGAATTTTCTGTATGAGGTTTTGC-3′	Sigma-Aldrich	N/A
Deposited data		
NGS dataset from phage display peptide library screenings	Zenodo	https://doi.org/10.5281/zenodo.14871106

Continued

REAGENT or RESOURCE	SOURCE	IDENTIFIER
Software and algorithms		
R (3.6.3 and 4.1.1)	R Foundation	https://www.r-project.org/
Ingenuity Pathway Analysis	QIAGEN	https://digitalinsights.qiagen.com/products-overview/discovery-insights-portfolio/analysis-and-visualization/qiagen-ipa/
RCSB Protein DataBank	Research Collaboratory for Structural Bioinformatics	https://www.rcsb.org/
PEP-FOLD2	Resource Parisienne in BioInformatique Structurale	https://mobyle2.rpbs.univ-paris-diderot.fr/cgi-bin/portal.py#forms::PEP-FOLD
UCSF Chimera	Resource for Biocomputing, Visualization, and Informatics (University of California, San Francisco)	https://www.cgl.ucsf.edu/chimera/
GROMACS (2019.6 and 2020.3)	GROMACS	https://www.gromacs.org/
OpenMM (8.0.0)	Stanford University	https://openmm.org/
Prism 9	GraphPad	https://www.graphpad.com/
Other		
Captive bolt gun apparatus	Ramset Karl Schermer Company	Model RS22 Model KC
SfiI restriction enzyme	New England Biolabs	Cat#R0123L
Bg1I restriction enzyme	Boehringer Mannheim	Cat#404101
T4 DNA ligase	Invitrogen	Cat#15224041

EXPERIMENTAL MODEL AND SUBJECT DETAILS

Animals

Female Sinclair miniature pigs (*Sus scrofa domesticus*) (Sinclair Bio Resources, Auxvasse, MO) and female Sprague-Dawley rats (*Rattus norvegicus*) (MPI Research, Mattawan, MI) were commercially obtained. All protocols used in this study were reviewed and approved by their corresponding Institutional Animal Care and Use Committee (IACUC). The targeting study protocols were reviewed and approved by the IACUCs of the University of Texas M.D. Anderson Cancer Center and of the U.S. Army Institute of Surgical Research (Fort Sam Houston, TX) in compliance with the Animal Welfare Act and Animal Welfare Regulations. Moreover, the principles of the Three Rs (Replacement, Reduction and Refinement) and the ARRIVE guidelines were followed. Finally, all animals received care in compliance with the 1996 *Guide for the Care and Use of Laboratory Animals* by the National Research Council and were maintained in an Association for Assessment and Accreditation of Laboratory Animal Care International-accredited facility. The imaging protocols in pigs were reviewed and approved by the IACUC of the Western University and the University of Guelph, according to the Ontario Animals for Research Act and the guidelines of the Canadian Council on Animal Care. Imaging studies were reviewed and approved by Invicro and performed at the Lawson Health Research Institute (London, Ontario, Canada). The imaging protocols in rats were reviewed and approved by Invicro and performed at an MPI Research testing facility (Mattawan, MI).

METHOD DETAILS

Porcine model of compound femur fracture and hemorrhagic shock

The reproducible porcine model of compound femur fracture and hemorrhagic shock has been described.[14] In brief, the animals were initially sedated with 8 mg/kg of Telazol (50 mg/mL of tiletamine hydrochloride and 50 mg/mL of zolazepam hydrochloride) plus 1.2 mg of atropine, both administered intramuscularly (IM). The animals were then positioned supine, intubated with a cuffed endotracheal tube, fully anesthetized with 4% inhaled isoflurane in 100% O_2, and mechanically ventilated (initial tidal volume, 10 mL/kg body weight; peak pressure, 20 cm H_2O; rate,10–12 breaths/min to preserve a baseline end-tidal P_{CO2} of 40 ± 2 mmHg, along with intermittent sigh breathing), and inhaled isoflurane for anesthesia maintenance was titrated between 1% and 3%, with general anesthesia depth clinically monitored according to response to pinch; epidural anesthesia was also performed with bupivacaine to ensure that adequate analgesia. A 5-French arterial catheter was inserted into the corresponding femoral artery by using a cutdown technique for regular monitoring of arterial blood pressure. By using a 14-gauge needle, the mid-femur was localized, and a small cruciate

incision was made. Then, a standard injury was created with a captive bolt gun apparatus (Model RS22, Ramset, Glendale Heights, IL or Model KC, Karl Schermer Company, Paderborn, Germany) with a mushroom-shaped head applied to the medial hindleg and fired to induce a compound femur fracture. During extensive logistic and optimization experiments, consistent positioning and practice of the bolt gun apparatus enabled recapitulation of acute trauma involving a compound femur fracture. These procedures were systematically planned and meticulously executed at contracted facilities, namely the U.S. Army Institute of Surgical Research (Fort Sam Houston, TX) and the Lawson Health Research Institute (London, Ontario, Canada)

Phage display library preparation

Non-commercial random phage libraries displaying cyclic CX_7C and CX_8C peptides (X, any of the 20 natural amino acid residues, flanked by cysteines forming a disulfide bridge under oxidizing conditions) on the pIII minor coat protein were constructed by encoding degenerate synthetic oligonucleotides into the pIII gene as previously described.[63,64] With this approach, each phage clone displays up to five copies of a random, cyclic peptide comprised of seven or eight amino acids flanked by cysteine residues.

Briefly, the fUSE5 phage plasmid (100 ng) was electroporated into ElectroMAX DH5α-E competent cells (Invitrogen, Cat#11319019) and plated on Luria Broth (LB) agar plates containing 40 μg/mL of tetracycline. A starter culture inoculum was expanded in 10 L of LB media containing 40 μg/mL of tetracycline, and plasmid purification was performed by using a two-step process: Plasmid Plus Giga Kit (QIAGEN, Cat#12991) procedure, followed by a cesium chloride (CsCl)/ethidium bromide gradient. For every 3 mL of plasmid (corresponding to 5–10 mg) in TE buffer, 3.2 g of CsCl and 400 μL of ethidium bromide (10 mg/mL) were added. The mixture was centrifuged at 100,000×g for 16 h at 25°C, and the DNA band was extracted using an 18-gauge needle. Ethidium bromide was removed through three rounds of organic extraction with an N-butanol/1M NaCl solution. CsCl was removed by dialyzing the DNA in 5 L of TE buffer by using a 10,000 Da molecular weight cutoff dialysis cassette. The plasmid was ethanol-precipitated and resuspended in double-distilled water, and the DNA concentration and purity were measured, wherein OD_{260} = 1 corresponds to 50 μg/mL of double-stranded DNA. The fUSE5 plasmid was digested with the *SfiI* restriction enzyme (New England Biolabs, Cat#R0123L), purified by using the QIAquick PCR Purification Kit (QIAGEN, Cat#28106), and eluted in 50 μL of 10 mM Tris-HCl (pH 8.5).

Synthetic single-stranded degenerate oligonucleotides were converted into double-stranded DNA libraries by using Sequenase DNA polymerase (Amersham, Cat#70770). In a 10-μL reaction containing 2 μg of oligonucleotides and 4 μg of fUSE5 primers in buffer, the mixture was incubated at 65°C for 2 min, then ramped down to 40°C for 10 min, then placed on ice. The oligonucleotides were purified by using the QIAquick Nucleotide Removal Kit (QIAGEN, Cat#28306). A 50-μL elongation reaction was performed with 2 μL of 10 mM dNTP, 5 μL of 0.1 M dithiothreitol (DTT), 31 μL of enzyme dilution buffer, and 2 μL of Sequenase DNA polymerase at 37°C for 1 h. Double-stranded oligonucleotides were digested with *Bg1I* restriction enzyme (40 U/μL) (Boehringer Mannheim, Cat#404101) and purified by using the QIAquick Nucleotide Removal Kit. Inserts were ligated into the linearized fUSE5 plasmid by using T4 DNA ligase (Invitrogen, Cat#15224041), with molar ratios (plasmid:insert) ranging from 1:1,000 to 1:1 and tested for optimal efficiency. Ligation reactions were incubated overnight at 16°C and purified with the QIAprep Spin Miniprep Kit (QIAGEN, Cat#27104).

Purified plasmids were electroporated into MC1061 competent *E. coli* by using the following settings: 300 μF, 4 kΩ resistance, low-Ω DC voltage, and a fast charge to 420 V. After transformation, the libraries were amplified in 10 L of LB media containing tetracycline in an orbital shaker at 37°C for 16 h. The culture was centrifuged twice at 7,000×g for 20 min, and the supernatant was collected. Phage particles were precipitated by adding 4% (w/v) PEG 8000 and 3% (w/v) NaCl and stirring overnight (ON) at 4°C. The supernatant was centrifuged at 14,000×g at 4°C for 20 min, and the phage pellet was resuspended in 150 mL of Tris-buffered saline (TBS). A second PEG/NaCl precipitation was performed on the supernatant, followed by ON incubation at 4°C. The phage pellet was then resuspended in 10–50 mL of TBS.

Endotoxin removal was performed for the phage library preparation before *in vivo* experimentation. Per each 1.5 mL of phage library solution, 15 μL of 10% Triton X-114 in endotoxin-free water were added and incubated on ice for 10 min. Each solution was then warmed to 37°C for 10 min followed by removal of the Triton X-114 phase by centrifugation at 14,000 rpm for 1 min. This process was repeated at least four times. Endotoxin-free phage solution was precipitated in 35 mL of phosphate-buffered saline (PBS) containing 5 mL of PEG/NaCl at 4°C for 4 h, followed by centrifugation at 14,000 rpm at 4°C for 30 min. The phage preparation was solubilized in PBS and filtered with a 0.45-μm pore size filter. The levels of endotoxin were measured by using the Kinetic-QCL Kinetic Chromogenic LAL Assay (Lonza Bioscience, Cat#50-650U). Phage preparations with <0.05 EU/mL of endotoxin were used in this study.

In vivo phage display library screenings

An admixture (1:1) of random phage libraries displaying cyclic CX_7C and CX_8C peptides was used at a total dose of 10^{12} TU (i.e., 5× 10^{11} TU for each library), diluted in 150 mL of normal saline. This library admixture was IV infused over 1 h in a serial cohort of negative control animals (non-injured pigs, n = 4). To determine the baseline phage particle distribution, arterial blood samples were obtained at multiple time points in addition to necropsy samples from several tissues (n = 13; aorta, bone marrow, bone, brain, fat, heart, kidney, liver, lung, muscle, pancreas, skin, and spleen). Prior to the induction of the injury in the femur fracture model (experimental pigs, n = 4), blood and muscle biopsy samples were taken as baseline measurements. Once the baseline biopsies were obtained, each experimental animal was injured as described above. Immediately following injury, the experimental animals received the library

admixture dose under the same conditions. Arterial blood samples and paired biopsy samples from the injury site (fractured femur) plus the contralateral intact hindleg were recovered with serial 14-gauge needle biopsy at fixed time points (1, 10, 60, 70, and 120 min). Tissue samples (n = 13) were taken at necropsy as described above.

All obtained samples were promptly frozen and total DNA was extracted through the DNeasy Blood and Tissue Kit (QIAGEN, Cat#69504). Phage particles in select samples were quantified as relative TU via K91 *E. coli* infection or quantitative real-time PCR (FW: 5′-TGAGGTGGTATCGGCAATGA-3′; RV: 5′-GGATGCTGTATTTAGGCCGTTT-3′) via amplification of the phage-encoded TetR gene as described.[5,10,16] DNA encoding peptide inserts originating from samples of the injured pigs was amplified via PCR (FW: 5′-CGCAATTCCTTTAGTTGTTCC-3′; RV: 5′-TGAATTTTCTGTATGAGGTTTTGC-3′) and underwent NGS via 454 GS FLX as described.[16]

Bioinformatic analysis of homing peptides

The bioinformatics approach to analyze displayed peptide-encoding DNA reads obtained via NGS has been described.[5,10,16] An initial round of analysis of nucleotide sequencing results served to remove low-quality, incomplete, or stop codon-containing peptide reads and to assemble the repertoire of peptide sequences. Saturation plots assessing distinct peptide sequences were generated via random shuffling and sampling of the recovered peptide sequences (excluding singlets) in sets of 100 recovered peptide sequences [except for one group with a value of (n mod 100), where n is the total number of recovered peptide sequences for a sample not divisible by 100] by using R (version 3.6.3).[65] A total of 100 rounds of random shuffling was performed and the mean number of distinct peptide sequences per sample in each set of recovered peptides are graphed in the displayed saturation plots. A large-scale subtractive clustering analysis of the recovered motifs was then performed. The peptide sequences obtained from the experimental and control tissues were clustered as biologically similar groups with permitted mismatches. First, correlative (e.g., injured muscle samples from all biopsy time points), non-correlative (e.g., injured muscle samples from biopsies and necropsy), and anti-correlative (e.g., injured and non-injured muscle samples) relationships between the sets were defined for statistical testing based on tissue-specific features and used for subtraction analysis. Next, peptide-encoding sequences were filtered by statistical significance calculated for clusters from injured versus contralateral intact (non-injured) control tissues belonging to negatively-correlated sets based on the number of appearances. Sequences with $p < 0.05$ according to Fisher's exact test (one-sided) and adjusted for multiple comparisons by using false discovery rate (FDR) were designated for initial clustering. Subsequently, peptides were clustered to identify motifs of at least three amino acid residues (no gaps allowed), and then refined via extension into patterns of four, five, and six amino acids (gaps allowed). Patterns were then filtered by statistical significance (i.e., number of appearances in injured versus corresponding non-injured tissue samples, set at $p < 0.05$ and adjusted for multiple comparisons by using FDR). The remaining peptide clusters were next prioritized based on the total number of matching sequences and processed for multi-scale sequence alignments. Finally, high-throughput BLASTP was performed with selected motifs to identify matches grouped by clusters or patterns, and peptides were aligned to native protein hits. The final curation of peptide sequence alignments was manually supervised to ensure internal consistency.

Peptide synthesis and radiolabeling

All synthetic cyclic peptides (n = 23, Table 1) were generated by solid-phase (Merrifield) synthesis, purified, and quality-controlled at CPC Scientific (Sunnyvale, CA).

^{89}Zr was purchased from 3D Imaging LLC (Little Rock, AR). Desferoxamine (DFO)-conjugated CRQRPASGC and control peptide (DFO-KK-PEG2-CRQRPASGC-PEG2-KK and DFO-KK-PEG2-CRQR<u>A</u>ASGC-PEG2-KK, respectively) were labeled with ^{89}Zr at the University of Massachusetts Medical School (Worcester, MA). Briefly, the ^{89}Zr was transferred to a glass vial, and while gently shaking, 1 M oxalic acid was added to the vial, followed by 110 μL of 2 M sodium carbonate. The sample was left for 3 min at room temperature (RT). Then, with gentle shaking, the following were added successively to the vial: 0.3 mL of 0.5 M HEPES (pH 7.1), DFO-peptide (10 mg/mL in saline), and finally a second aliquot of 0.5 mL of 0.5 M HEPES (pH 7.1). The final pH of the labeling reaction was within the range of 6.8–7.2. The sample was left at RT for 1 h. Radiolabeling efficiency was determined by C8 reverse-phase, high-performance liquid chromatography (RP-HPLC).

Dodecane tetraacetic acid (DOTA)-conjugated CRQRPASGC was radiolabeled with ^{111}In by MPI Research (Mattawan, MI). Briefly, to 2.1 mg DOTA-labeled CRQRPASGC, 150 μL of 1 N HCl was added to adjust the pH to ~5. To 10.42 mCi of ^{111}In-Cl3 in 450 μL of 0.6 M ammonium acetate (pH 7), then 100 μL 0.6 M ammonium acetate was added to achieve pH 5. To each 1.8 mL Cryovial, 100 μL (175 μg) of DOTA-labeled CRQRPASGC was added, followed by 320 μL (~5 mCi) of ^{111}In. Tubes were incubated in 0.6 M ammonium acetate buffer (pH ~5) at 45° C for 90 min, then at 65° C for 90 min. The radioactive purity of the final product was ~95% and the specific activity of ^{111}In-DOTA-CRQRPASGC was ~0.03 mCi/μg.

Affinity chromatography and phage-binding assays

Targeted peptides were individually coupled to BcMag long-arm amine-terminated magnetic beads (Bioclone, Cat#FA-115) at 5 mg of peptide per 1 mL of beads. Solubilized tissues (experimental injured or non-injured controls) (10 mg in 10 mL of extraction buffer) were applied to the beads and bound proteins were eluted with glycine, pH 2.8. Eluates were subjected to clean-up and two-dimensional sodium dodecyl sulfate-polyacrylamide gel electrophoresis (SDS-PAGE) under reducing conditions and proteins were visualized with SYPRO Ruby Protein Gel Stain (Invitrogen, Cat#S12000). Unique protein bands (i.e., those that were not observed in a

matching receptor isolation from control pig tissue for each peptide) were excised and analyzed by matrix-assisted laser desorption/ionization coupled to time-of-flight (MALDI-TOF) mass spectrometry. Identified proteins from the *Sus scrofa* proteome were categorized according to the Protein ANalysis THrough Evolutionary Relationships (PANTHER) Classification System.[66]

Peptide-targeted phage-binding assays to human recombinant proteins, including CALR (OriGene, Cat#TP303222; Abnova, Cat#H00000811-P01), CASQ1 (Abnova, Cat#H00000844-P01), HSP27 (ATGen, Cat#ATGP0444), HSP22 (bioWORLD, Cat#22060349-1), and CRYAB (Abcam, Cat#ab48779) or negative control (bovine serum albumin, BSA), were performed as described.[5,10] Briefly, 100 ng of each protein dissolved in 50 μL PBS were immobilized in microtiter wells at 4°C ON, washed twice with PBS, blocked with PBS containing 3% BSA at RT for 1 h, and incubated with targeted or insertless phage in 50 μL of PBS containing 1.5% BSA. After 2 h incubation at RT, wells were gently washed with PBS, and phage particles were recovered by bacterial infection. For the peptide-targeted phage-binding assay to immunocaptured CASQ, 10 μg/mL of anti-CASQ antibody (Invitrogen, Cat#MA3-913) in 50 μL PBS were immobilized in microtiter wells at 4°C ON, blocked with 2% BSA at RT for 2 h, and incubated with cell extract in 50 μL at 4°C ON. The wells were then incubated at RT for 1 h, washed three times with PBS, and incubated with targeted phage in 50 μL. After 2 h incubation at RT, wells were gently washed with PBS, and phage particles were recovered by bacterial infection. Serial phage-binding assays were evaluated with or without (i) the corresponding synthetic peptide (0, 100, or 1,000 ng/μL), (ii) EDTA (1 mM), (iii) Ca²⁺ (0, 0.5, or 1 mM), or (iv) a polyclonal anti-CALR antibody (Abcam, Cat#ab14234), as indicated. Phage binding was evaluated by relative TU counting.

In silico exploration of relationships between Ca²⁺ and candidate receptors

Ingenuity Pathway Analysis (IPA) (QIAGEN)[67] was used (i) to determine the relationship between each of the proteins (n = 82) identified by MALDI-TOF and Ca²⁺, and (ii) to visualize the interaction network containing Ca²⁺ and each of the following candidate receptors (n = 20): CASQ1, HSP27 (HSPB1), CRYAB, GC1QBP, DES, HSPA5 (HSC70), CALU, PPIB, PRDX3, LTF, ALDOA, HSPA8 (BIP), ANXA1, BAG3, HRG, CALR, COL11A2, CSTA, SEC31A, and CTSG. Briefly, a new pathway was initiated, in which the proteins as Genes and Chemical symbols were added. Ca²⁺ symbol (considered "chemical – endogenous mammalian") was also added. Path Explorer was executed with the polypeptide entities in Set A and Ca²⁺ in Set B. Parameters included: (i) only direct interactions, (ii) information limited to the Ingenuity Knowledge Base, (iii) Ingenuity Expert Information as the data source, (iv) only experimentally observed for confidence level, (v) multiple species (human, mouse, rat, and uncategorized), (vi) all tissues and cell lines, (vii) all mutations, (viii) chemical-protein interactions and protein-protein interactions as relationship types, (ix) January 1954 to December 2023 as publication date range (including unspecified publication date), (x) relevant node types (complex, cytokine, enzyme, fusion gene/product, GPCR, group, growth factor, ion channel, kinase, ligand-dependent nuclear receptor, peptidase, phosphatase, transcription regulator, translation regulator, transmembrane receptor, transporter, other), (xi) all diseases, and (xii) all biofluids. In our study, interactions found under "Shortest path" were represented as "Direct," while interactions found under "Shortest path +1" (i.e., exactly one protein mediator) were represented as "Indirect."

Tissue immunohistochemistry

Tissue samples were obtained from the injured and non-injured control sites via serial biopsies post-injury or at necropsy. The biopsies were fixed, paraffin-embedded, and processed for histology. Tissue sections (5 μm) were deparaffinized, rehydrated, and blocked for endogenous peroxidases and for nonspecific protein binding (Agilent Dako, Santa Clara, CA). For phage overlay assays, tissue sections were incubated with CRQRPASGC-displaying or insertless phage particles (5×10⁸ phage particles/mL) as previously described.[68] After washes with PBS containing 0.05% Tween 20 (PBST), the slides were incubated with the primary rabbit anti-fd bacteriophage antibody (Sigma-Aldrich, Cat#B7786 at 1:800) followed by incubation with anti-rabbit horseradish peroxidase (HRP)-conjugated secondary antibody (Jackson ImmunoResearch, Cat#111-035-003). For Ca²⁺ staining, Alizarin Red S (Sigma-Aldrich, Cat#A5533) was used as described.[69] For receptor staining, primary antibodies included chicken anti-CALR antibody (Abcam, Cat#ab14234 at 1:200) and rabbit polyclonal anti-CASQ1/2 antibody (Abcam, Cat#ab3516 at 1:200) and secondary antibodies included anti-chicken (Jackson ImmunoResearch, Cat#703-035-155) and anti-rabbit HRP-conjugated antibodies (Jackson ImmunoResearch, Cat#111-035-003).

Homing and molecular imaging of targeted or mutant ligand peptide

Prior to the injury induction, biopsy samples were taken at baseline. The pigs received either CRQRPASGC-displaying phage (n = 2 pigs) or insertless control phage (n = 2 pigs) diluted in 100 mL of normal saline IV over a period of 1 h. The femur fracture was then induced, and serial biopsies were collected from both injured and contralateral intact hindleg muscles up to 120 min. The animals were euthanized at 240 min and tissue samples were also collected at necropsy. Phage homing was evaluated by qPCR and immunohistochemistry. For qPCR, four technical replicates per time point per hindleg per animal were averaged to yield a single value for each combination. Relative values were calculated based on qPCR values of a dilution of administered phage per animal in order to facilitate direct comparison between animals.

All synthetic peptide labeling and molecular imaging experiments reported here were performed by a contract research organization (Invicro, Needham, MA) at an MPI Research Facility (Mattawan, MI) or the Lawson Health Research Institute (London, Ontario, Canada) according to our specifications and under our supervision, unless otherwise specified.

As the first molecular imaging study, PET/MRI in a porcine model of acute traumatic femur injury was performed by using ^{89}Zr-labeled peptides. Sinclair miniature pigs ($n = 5$ per experiment) were assigned into three groups: (i) control with no injury ($n = 1$) receiving ^{89}Zr-labeled CRQRPASGC, (ii) experimental with injury ($n = 2$) receiving ^{89}Zr-labeled CRQRPASGC, and (iii) experimental with injury ($n = 2$) receiving ^{89}Zr-labeled CRQRAASGC control peptide. Immediately following the standard femur fracture as described above, the animals were positioned in an integrated PET/MRI (Siemens Biograph mMR, Munich, Germany), and the ^{89}Zr-labeled peptides were administered IV. The target mass dose was 15 μg/kg at a target radioactivity dose of 3 mCi. PET imaging data were acquired continuously for 6 h following injection of the peptides, with a single MRI acquired at the beginning of each PET sequence. PET fields-of-view alternated for a total of three whole-body scans (for internal quality assurance and quality control) and nine focused pelvic and femoral scans: 0–90 min (focused hindlegs), 90–120 min (whole body), 120–210 min (focused hindlegs), 210–240 min (whole body), 240–330 min (focused hindlegs), and 330–360 min (whole body). During the procedure, IV fluids were administered at a maintenance rate and arterial blood pressure was continuously monitored. Upon completion of the imaging, each animal was euthanized while still under deep general anesthesia with an IV bolus of potassium chloride. Tissue samples were collected from soft tissues in the control and affected hindlegs and preserved in formalin. All samples and carcasses were stored in a shielded radioactivity isolation room until they decayed to the background levels. PET/MRI data were quantitatively analyzed to compare the uptake and concentration of the labeled peptides at the injury site and non-injured hindleg. MRI data were stitched together to generate a whole-body MRI scan. Next, the MRI data was resampled to the voxel size of the PET image (2.00 mm isotropic resolution) and co-registered. The focused fractured and control femur datasets were also co-registered between MRI and PET. For whole-body region of interest (ROI) generation (as internal quality assurance and quality control), a small, fixed-volume ROI was placed in a region of homogeneous uptake in the liver and muscle; for the heart, kidneys, bladder, gallbladder, stomach and intestines, regions were segmented to include all of the signals in each of the respective regions. For fractured and control femur imaging generation, ROIs were placed for one time point for each animal at the area of injury plus any areas of soft tissue uptake. To account for uptake in the periosteum and growth plate, a spherical ROI was placed at the fracture site and at the corresponding site in the opposite hindleg. ROIs for the other time points were generated by registering each animal to its subsequent time points. Additional ROIs were placed on the side of the control animal (without fracture) in similar locations and volumes as a comparison. Maximum-intensity projections (MIPs) for each animal and each time point were generated, and scaled to the percent of the injected dose per gram (% ID/g). In addition, flythrough images showing the fracture in the MRI, and also the MR plus PET imaging were generated.

For a second independent experimental model of major trauma in rats, SPECT/CT was performed with ^{111}In-DOTA-labeled CRQRPASGC. Female Sprague-Dawley rats (*Rattus norvegicus*) received a single-dose of 0.05 mg/kg buprenorphine via subcutaneous (SC) and were subsequently fully anesthetized with 2–5% isoflurane (induction) and 2–3% isoflurane (maintenance) throughout the study. Once the rats ($n = 4$) were anesthetized, complete fracture of the femur bone along with soft tissue damage in one hindleg was induced ($n = 3$) at a contracted facility, namely an MPI Research testing facility (Mattawan, MI), as described above for the pigs. ^{111}In-DOTA-CRQRPASGC (∼30 μg) was administered IV (tail vein) immediately after injury with the rats placed on the bed of the SPECT/CT scanner. The acquisition of SPECT images was initiated simultaneously with the administration of ^{111}In-DOTA-CRQRPASGC peptide radiotracer. Animals underwent imaging of whole body (for internal quality assurance and control) and focused regions from 0 to 5 h according to the following imaging protocol: 0–18 min (focused, planar), 20–60 min (whole-body, semi-dynamic SPECT), 1–2 h (focused SPECT), 2–3 h (whole-body SPECT), 3–4 h (focused SPECT), 4–5 h (whole-body SPECT). Of note, a fourth injured rat moved during the SPECT portion of this experiment, hence the SPECT scan could not be co-registered to the CT scan; this animal was therefore excluded from the study. A non-injured rat receiving ^{111}In-DOTA-CRQRPASGC served as the negative control ($n = 1$). Upon completion of the imaging study, both hindlegs (injured and non-injured) were resected, fixed in formalin, with their carcasses stored in a shielded radioactivity isolation room until decayed to the background level. To assess the whole-body distribution and kinetics of ^{111}In-DOTA-CRQRPASGC for internal quality assurance and quality control, ROIs corresponding to the following organs and tissues were defined: heart, liver, lungs, kidneys, bladder, brain, muscle, and whole body. These ROIs were acquired in one of two manners, namely either hand-drawn or by fitting a pair of ellipsoids of fixed volume to the region. Fixed-volume analysis was used for the heart (as a surrogate endpoint of the blood pool), liver, lung, kidneys, and brain. The muscle ROI was hand-drawn and is a small section of the forelimb muscle; thus, the total activity does not represent the activity of all rat muscles. Bladder ROIs were segmented by initially setting a minimum threshold of ∼3% of the maximum voxel and then dilating the ROI by two voxels in every direction.

To compare the uptake in the injured and non-injured hindlegs of the rats, the focused hindleg images were used. Injured and non-injured hindleg ROIs were defined. A hand-drawing technique was used to specifically avoid artifacts present in the image data caused by very high uptake in the bladder and residual contamination on the fur caused by excretion. For analysis of the focused hindleg planar data, summed images were generated from each dynamic planar sequence by summing up 540 individual time frames. Summed images were manually registered to one another. Landmarks, including the bladder, tail, and knees where possible, were identified and used to define left and right thigh ROIs in the sum planar scans. Due to low count rates for all planar scans, a sliding window approach was used to generate time-activity curves from the left and right ROIs for each scan. In this approach, data from a 1-min window (30 frames) were integrated to generate a single point on the curve. This 1-min window was then moved in 20 s (10-frame) increments to generate the entire curve.

Optical methods: Fluorescence emission spectroscopy and circular dichroism

For fluorescence emission spectroscopy, CALR at a concentration of 1 μM in TBS (20 mM Tris-HCl, pH 7.4, 150 mM NaCl) in the presence or absence of 1 mM CaCl₂ was titrated in with 150 μM (final molar concentration) of each experimental or control peptide. The steady-state intrinsic fluorescence of CALR was recorded from 300 nm to 400 nm with excitation at 280 nm and 295 nm.

For circular dichroism (CD), spectra of 8 μM of CALR in 10 mM sodium phosphate (pH 7.4) were recorded in the presence or absence of 50 μM or 400 μM of experimental or mutant peptide. All spectra were corrected for background signal by subtraction of the appropriate blanks (i.e., buffer or low-concentration peptide signals).

CALR interactors and structural modeling of the CRQRPASGC-CALR complex

IPA[67] was applied to assemble a list of all known protein interactors of CALR. Briefly, a new pathway was initiated, in which CALR as a Genes and Chemicals symbol were added. The Grow function was executed. Parameters included: (i) only direct interactions (including all molecules or canonical pathways upstream or downstream), (ii) information limited to the Ingenuity Knowledge Base, (iii) Ingenuity expert information as the data source, (iv) only experimentally observed for confidence level, (v) multiple species, (vi) all tissues and cell lines, (vii) all mutations, (viii) protein-protein interactions as relationship types, (ix) January 1954 to December 2023 as publication date range (including unspecified publication date), (x) relevant node types (complex, cytokine, enzyme, fusion gene/product, GPCR, group, growth factor, ion channel, kinase, ligand-dependent nuclear receptor, peptidase, phosphatase, transcription regulator, translation regulator, transmembrane receptor, transporter, other), (xi) all diseases, and (xii) all biofluids. The list of proteins was exported, and the corresponding UniProt accession numbers were retrieved. BLASTP was performed with all UniProt accession numbers inputted as the subject and RQRPASG inputted as the query.

For *de novo* peptide structure prediction, the amino acid sequence of the peptide CRQRPASGC was inputted into PEP-FOLD2[70] with a specified disulfide bridge between the flanking cysteine residues. Both 100-run and 200-run simulations were performed. The top-generated model (according to sOPEP energy) containing a disulfide bridge between flanking cysteine residues for each peptide was selected for further analysis. By using UCSF Chimera,[71] the CRQRPASGC peptide was structurally overlayed with TAPBP in its native complex with CALR (PDB ID: 6ENY)[32] according to best fit. The structural representation does not include the other molecules of the complex (i.e., β-2-microglobulin, protein disulfide-isomerase A3, HLA class I histocompatibility antigen A-3 α chain, and oligosaccharides).

Molecular dynamics simulations of CRQRPASGC and CALR

The methodology for molecular dynamics simulations used here has been described.[72,73] Briefly, explicit-solvent simulations of CRQRPASGC were produced by using the GROMACS 2020.3 software[74,75] with the AMBER99SB-ILDN protein force field.[76] The initial structure of the CRQRPASGC peptide was generated as described above. The peptide was solvated with TIP3P water molecules,[77] where the simulated box was defined to have a 10 Å buffer between the edge of the box and the peptide. To neutralize the simulated system, two chloride (Cl⁻) ions were introduced. First, a steepest-descent energy minimization was performed, followed by 5 ns of NVT and 5 ns of NPT simulations, at 300 K temperature, while positional restraints were imposed on all non-H atoms. Positional restraints were then removed, and steepest-descent energy minimization was performed. A second round of equilibration was then performed: 5 ns of NVT and 5 ns NPT simulations at 310 K temperature. The production simulation was then performed in the NPT ensemble for 1 μs. The NPT simulations ensemble implemented the Parrinello-Rahman barostat[78] with a reference pressure of 1 bar. All simulations used the Nose-Hoover thermostat.[79,80]

Simulations of CALR were performed by using the OpenMM 8.0.0 software package[81] with input files generated with GROMACS 2019.6 software[74,75] with the AMBER99SB-ILDN protein force field.[76] Because the C-terminal tail was not found to interact with the disordered loop comprised of residues L203–Y299 in the initial simulations, incorporated simulations included CALR (PDB: 6ENY)[32] without this region to reduce the computational load of the simulations. The protein was solvated with TIP3P water molecules,[77] where the simulated box was defined to have a 10 Å buffer between the edge of the box and CALR. For each Ca²⁺ molar concentration, the simulated system was neutralized by the introduction of either sodium (Na⁺) or Cl⁻ ions. In order to equilibrate the simulation, a steepest-descent energy minimization was performed, followed by 5 ns of NVT and 5 ns of NPT simulations, at 300 K temperature, while positional restraints were imposed on all non-H atoms. Positional restraints were then removed, and steepest-descent energy minimization was performed. A second round of equilibration was then performed: 5 ns of NVT and 5 ns NPT simulations at 310 K temperature. Finally, 100 ns of NPT simulations were performed to permit ion equilibration. The production simulation was then performed in the NPT ensemble. The ensemble of NPT simulations implemented the Parrinello-Rahman barostat[78] with a reference pressure of 1 bar. All simulations used the Nose-Hoover thermostat.[79,80] For each Ca²⁺ molar concentration, four replicas were performed, each corresponding to approximately 500 ns. The displayed results were derived from the aggregated simulation for each Ca²⁺ molar concentration.

QUANTIFICATION AND STATISTICAL ANALYSIS

Data were plotted with GraphPad Prism 9 or R (version 3.6.3). Statistical tests were performed by using GraphPad Prism 9 or R (version 4.1.1)[65] with the R Commander interface.[82,83] Data are presented as mean ± SEM unless otherwise indicated. For phage-homing experiments, two-way ANOVA was performed with two factors (i.e., time point and hindleg). For phage-binding

assays, two- and three-way ANOVAs were performed with two factors (i.e., phage construct and immobilized protein) and three factors (i.e., phage construct, immobilized protein, and either cognate peptide concentration, presence of EDTA, $CaCl_2$ concentration, or presence of anti-CALR antibody), respectively. Statistical significance for post hoc Bonferroni's multiple comparisons test was set at $\alpha = 0.05$ with multiplicity-adjusted p-values as indicated. As previously noted, bioinformatic analysis of individual peptide sequences and peptide clusters incorporated Fisher's exact test, wherein statistical significance was set at $\alpha = 0.05$ for FDR-adjusted p-values. Data were not eliminated during the conduction of the study or analyses except for the following instance: a fourth injured rat moved during the SPECT portion of the molecular imaging experiment, and hence the SPECT scan could not be co-registered to the CT scan. The animal was not able to be properly evaluated at all fixed time points throughout the experiment and was therefore excluded from the corresponding section of the study (Figures S6A and S6B).